# Variability and redistribution of heat in the Atlantic Water boundary current north of Svalbard

**A. H. H. Renner[1], A. Sundfjord[2], M. A. Janout[3], R. B. Ingvaldsen[4], A. Beszczynska-Möller[5], R. S. Pickart[6], M. D. Pérez-Hernández[6,7]**

[1]Institute of Marine Research, Tromsø, Norway
[2]Norwegian Polar Institute, Fram Centre, Tromsø, Norway
[3]Alfred Wegener Institute, Helmholtz Centre for Polar and Marine Research, Bremerhaven, Germany
[4]Institute of Marine Research, Bergen, Norway
[5]Institute of Oceanology, Polish Academy of Sciences, Sopot, Poland
[6]Woods Hole Oceanographic Institution, Woods Hole, MA, USA
[7]Division Environment, Marine and Freshwater Research Institute, Reykjavik, Iceland

**Key Points:**

- We present year-long records of hydrography and currents of the Atlantic Water boundary current north of Svalbard.
- Upper ocean heat loss is 16 $\mathrm{W m^{-2}}$ annually with episodic heat loss of >100 $\mathrm{W m^{-2}}$ in autumn and winter.
- AW inflow drives 80% of heat content variability, with wind-induced mixing and tidal mixing the other main factors.

Corresponding author: Angelika Renner, `angelika.renner@imr.no`

**Abstract**

We quantify Atlantic Water heat loss north of Svalbard using year-long hydrographic and current records from three moorings deployed across the Svalbard Branch of the Atlantic Water boundary current in 2012-2013. The boundary current loses annually on average 16 $\mathrm{W m^{-2}}$ during the eastward propagation along the upper continental slope. The largest vertical fluxes of >100 $\mathrm{W m^{-2}}$ occur episodically in autumn and early winter. Episodes of sea ice imported from the north in November 2012 and February 2013 coincided with large ocean-to-ice heat fluxes, which effectively melted the ice and sustained open water conditions in the middle of the Arctic winter. Between March and early July 2013, a persistent ice cover modulated air-sea fluxes. Melting sea ice at the start of the winter initiates a cold, up to 100 m deep halocline separating the ice cover from the warm Atlantic Water. Semidiurnal tides dominate the energy over the upper part of the slope. The vertical tidal structure depends on stratification and varies seasonally, with the potential to contribute to vertical fluxes with shear-driven mixing. Further processes impacting the heat budget include lateral heat loss due to mesoscale eddies, and modest and negligible contributions of Ekman pumping and shelf break upwelling, respectively. The continental slope north of Svalbard is a key example regarding the role of ocean heat for the sea ice cover. Our study underlines the complexity of the ocean's heat budget that is sensitive to the balance between oceanic heat advection, vertical fluxes, air-sea interaction, and the sea ice cover.


## 1 Introduction

The Atlantic Water (AW) inflow through Fram Strait is the largest oceanic heat source to the Arctic Ocean [*Aagaard et al.*, 1987]. The West Spitsbergen Current (WSC) carries the AW northward in Fram Strait until it splits into several branches (Fig. 1): The upper-slope part crosses the Yermak Plateau northwest of Svalbard and enters the Arctic Ocean as the Svalbard Branch [*Aagaard et al.*, 1987]; the Yermak branch follows the western Yermak Plateau northward before turning east; and a third part recirculates in Fram Strait [*Beszczynska-Möller et al.*, 2012; *Rudels et al.*, 2014]. Time series from long-term mooring deployments show that the volume flux in the WSC core at 79° N is quite stable [*Beszczynska-Möller et al.*, 2012]. The fraction of recirculation in Fram Strait, however, varies seasonally [*Hattermann et al.*, 2016], which in turn likely affects the relative distribution of AW in the Yermak and the Svalbard Branches [*Schauer et al.*, 2004]. Further complicating the picture, observations and modelling studies indicate that a third branch crossing Yermak Plateau might be established in winter [*Gascard et al.*, 1995; *Koenig et al.*, 2017]. It is still unclear whether these branches merge again east of Yermak Plateau. The continuation of the AW inflow into the Arctic, however, is topographically controlled and predominantly follows the continental slope as part of the Arctic Circumpolar Boundary Current around the perimeter of the deep Arctic Ocean basin [*Aagaard*, 1989; *Rudels et al.*, 1999; *Aksenov et al.*, 2011].

The slope area north of Svalbard is recognised as an important region for modification of the AW boundary current [*Polyakov et al.*, 2017] and a potential hotspot for tidally-driven mixing [*Rippeth et al.*, 2015]. However, the northeastern region has been little studied. In a mooring study, *Ivanov et al.* [2009] document a clear seasonal cycle with warmer and saltier water in autumn than in spring. Ship-based hydrographic transects conducted during summer and autumn show that although the Svalbard Branch is always discernible northeast of Svalbard, it is highly variably in space and time [*Cokelet et al.*, 2008; *Våge et al.*, 2016; *Pérez-Hernández et al.*, 2017]. The variability seen in such quasi-synoptic surveys may in part be attributed to frontal instabilities leading to eddy formation. This distorts the mean flow and hydrographic structure and thus adds uncertainty to geostrophic transport calculations [*Våge et al.*, 2016; *Pérez-Hernández et al.*, 2017].

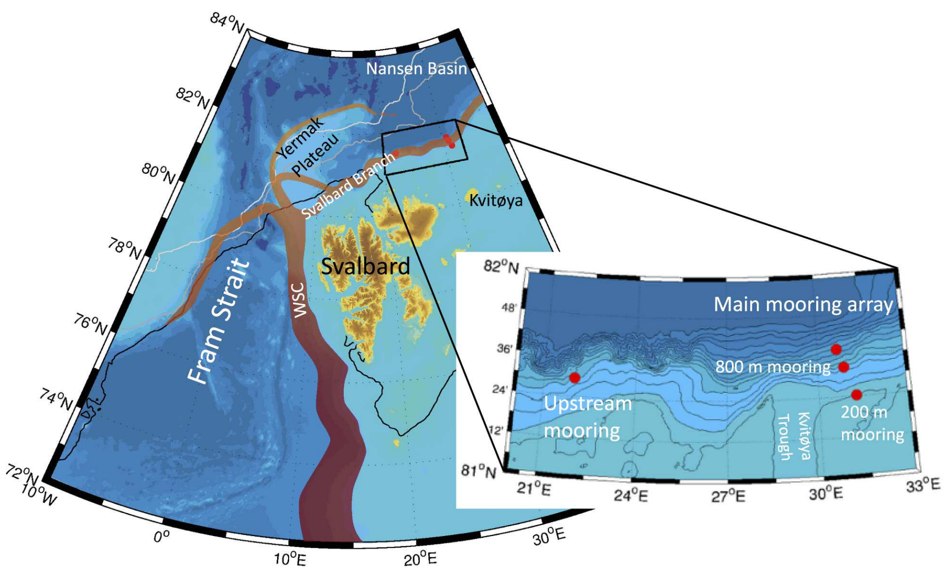


**Figure 1.** Map of the study region. The red lines on the overview map indicate the pathways of Atlantic Water flowing into the Arctic (WSC = West Spitsbergen Current). The black, dark grey, and light grey lines on the overview map denote the average position of the sea ice edge in March 2013, September 2012 and September 2013, respectively. Red dots in the inset show the positions of the moorings on the outer shelf and upper slope. Bathymetry is taken from IBCAO version 3.0 [*Jakobsson*, 2012].

The inflow of warm AW has a major impact on the sea ice cover north of Svalbard. The ice cover in this region is dominated by first- and second-year ice, either locally formed or advected into the area [*Renner et al.*, 2013]. However, the AW inflow provides enough heat to keep the area ice-free over prolongued periods of time [e.g. *Ivanov et al.*, 2016]. This ice-free region has been increasing to the east in recent years [*Vinje*, 2001; *Onarheim et al.*, 2014], likely as a result of increased oceanic heat transport [*Ivanov et al.*, 2012; *Onarheim et al.*, 2014; *Polyakov et al.*, 2017] which strongly affects a thinning ice cover [*Hudson et al.*, 2013; *Koenig et al.*, 2016; *Provost et al.*, 2017]. Observations from the upstream areas over Yermak Plateau and the slope north of Svalbard document large upward heat fluxes above the AW layer of several tens of $\mathrm{Wm^{-2}}$ well below the surface [*Meyer et al.*, 2017] and exceeding $100\,\mathrm{Wm^{-2}}$ in the under-ice boundary layer during strong wind events [*Peterson et al.*, 2017], or over the steep slope [*Koenig et al.*, 2016]. Away from the core of the boundary current, just beyond the continental slope, a late-summer study found boundary layer values ranging from near zero to more than $50\,\mathrm{Wm^{-2}}$ [mean $13.1\,\mathrm{Wm^{-2}}$, *Hudson et al.*, 2013]. This is likely in part driven by absorbed solar radiation but nevertheless is substantially higher than measurements from the interior Nansen Basin in winter [$2\,\mathrm{Wm^{-2}}$, *Meyer et al.*, 2017].

Previous studies have documented how inflowing pulses of warm water from the North Atlantic travel around the Arctic Ocean basin with the boundary current [*Polyakov et al.*, 2005] with significant impact on the Arctic sea ice cover [*Polyakov et al.*, 2010, 2017]. Recent measurements from the Eastern Eurasian Basin (EEB) have shown that the vertical stability of the boundary current may be weakening, allowing more heat to melt the overlying sea ice in that part of the ocean [*Polyakov et al.*, 2017]. Mooring data have provided significant insight on the vertical current structure [*Pnyushkov et al.*, 2013], seasonal and inter-annual variability of the temperature of the AW boundary current [*Dmitrenko et al.*, 2006; *Pnyushkov et al.*, 2015] and the signature of tides over the slope in the EEB [*Pnyushkov and Polyakov*, 2012]. Ship-based campaigns in the same area have documented cross-slope hydrographic properties [*Dmitrenko et al.*, 2011] and vertical mixing rates [*Lenn et al.*, 2009].

In light of the ongoing changes in the Arctic climate system and associated impacts on ecosystems and carbon cycling, improved knowledge about the variability and along-stream modification of the AW in the boundary current north of Svalbard is needed. This paper presents the first full-year multi-mooring deployment in the Svalbard Branch, and focuses on the seasonality of vertical redistribution of heat. The observational data set, processing procedures, and metrics are presented in Section 2. Results follow in Section 3, with presentations of the overall variability of temperature, currents, and heat content in the upper water column in Section 3.1, along-slope heat loss in Section 3.2, air-sea heat fluxes and vertical mixing in Section 3.3, wind-driven vertical transports in Section 3.4, and, briefly, lateral transports in Section 3.5. The results are then discussed in Section 4 and summarised in Section 5.'

## 2 Methods

### 2.1 Mooring data

In September 2012, three moorings were deployed over the outer shelf / upper continental slope north of Kvitøya (81.5° N, 31° E) as part of the *Long-term variability and trends in the Atlantic Water inflow region* (A-TWAIN) project (see Fig. 1). The moorings were located at the 200, 500, and 800 m isobaths, and were equipped with temperature and conductivity sensors as well as current meters. Unfortunately, the 500 m mooring was lost, but the other two were recovered successfully in September 2013. For an overview of the sensors deployed and the data return see Table 1.

**Table 1.** Overview of instrumentation on the ATWAIN moorings.

| Mooring | Instrument | Depth [m] | Record start | Record end |
|---|---|---|---|---|
| A200 | Seabird SBE37 | 52 | failed | |
| | Seabird SBE37 | 104 | 16 Sep 2012 | 15 Sep 2013 |
| | RDI Workhorse ADCP 150 kHz, upward looking | 112 | 16 Sep 2012 | 15 Sep 2013 |
| | Seabird SBE37 | 131 | 16 Sep 2012 | 15 Sep 2013 |
| | Seabird SBE37 | 180 | 16 Sep 2012 | 15 Sep 2013 |
| A500 | lost | | | |
| A800 | Seabird SBE16 | 25 | 18 Sep 2012 | 16 Sep 2013 |
| | Seabird SBE16 | 49 | 18 Sep 2012 | 06 Sep 2013 |
| | RDI Workhorse ADCP 300 kHz, upward looking | 97 | 18 Sep 2012 | 03 Sep 2013 |
| | Seabird SBE37 | 101 | 18 Sep 2012 | 16 Sep 2013 |
| | Seabird SBE37 | 198 | 18 Sep 2012 | 16 Sep 2013 |
| | Nortek Continental ADCP 190 kHz, upward looking | 244 | 20 Sep 2012 | 16 Sep 2013 |
| | Nortek Continental ADCP 190 kHz, upward looking | 378 | failed | |
| | Seabird SBE37 | 399 | 18 Sep 2012 | 16 Sep 2013 |
| | Aanderaa RCM7 | 402 | 18 Sep 2012 | 16 Sep 2013 |
| | Seabird SBE37 | 751 | 18 Sep 2012 | 16 Sep 2013 |
| | Aanderaa RCM7 | 754 | 18 Sep 2012 | 16 Sep 2013 |
| | Seabird SBE53 | 851 | 18 Sep 2012 | 17 Sep 2013 |
| AUPSTREAM | Seabird SBE37 | 50 | 28 Sep 2012 | 20 Sep 2013 |
| | Moored McLane Profiler with Seabird SBE52 | 52-750 | 28 Sep 2012 | 20 Sep 2013 |

The temperature and conductivity measurements were calibrated using shipboard conductivity-temperature-depth (CTD) profiles obtained during the deployment and recovery cruises (Seabird SBE911; see *Våge et al.* [2016] and *Pérez-Hernández et al.* [2017] for details regarding processing and calibration, and for hydrographic sections taken during the cruises). The SBE37s were found to be in very good agreement with the CTD values at the corresponding depths, and no sensor drift was observed. The SBE16 conductivity values were adjusted to the CTD data collected from the ship. Again, sensor drift was negligible.

Data from the ADCPs were filtered for data points with low signal strength, high error velocity, or unrealistically high velocities ($\pm 3 \cdot$ standard deviation). On several occasions, the 800 m mooring was blown down by as much as ~150 m at the uppermost sensor due to strong currents. Magnetic deviation is substantial at high latitudes (around 18° at the main mooring array during this deployment period). Issues with compass calibration prevented using simple rotational adjustment by the deviation applicable during the measurement period. Instead, assuming that the along-shelf current should dominate the current record [e.g. *Nøst and Isachsen*, 2003], the ADCP and point current meter records were rotated such that the main direction of the observed current follows the direction of the local 200 and 800 m isobaths. To create a combined dataset of along- and across-slope currents from the two ADCPs on the 800 m mooring, we derived the currents along the major (along-slope) and minor (across-slope) principle axes of current variance for each ADCP. Using the depth layer between 52 and 76 m where the ADCP measurements overlap, we find that the lower instrument generally overestimates current speeds by almost 30% relative to the upper ADCP. For a conservative approach regarding current and transport estimates, we therefore scaled the lower ADCP to match the upper one and used the values from the upper instrument when both were available. The combined ADCP record of along- and across slope currents was then detided using a 40-hour, 7th order Butterworth filter, and averaged to obtain daily means.

An additional mooring was located 145 km to the west of the main mooring array (22° E) over the 800 m isobath. The core of the boundary current is typically found over the continental slope between the 700 and 1000 m isobaths [*Ivanov et al.*, 2009], hence the choice to maintain moorings in this depth interval at two locations along the slope. The upstream mooring contained a McLane Moored Profiler (MMP) with SBE52 sensor recording temperature, conductivity and pressure, and a three-axis acoustic current meter (ACM) which measured profiles of velocity. The MMP sampled over the depth range 52-750 m, while a Seabird SBE37 MicroCat measuring conductivity, temperature, depth was located 2 m above the MMP. The MMP obtained profiles at an average interval of 12 hours, while the CTDs recorded every 15 minutes. The MMP data were interpolated to a regular grid in the vertical (2 m spacing) and merged with the SBE37 data, subsampled in time to match MMP record.

### 2.2 Environmental data

Sea surface temperature (SST) was obtained from the Optimum Interpolation Sea Surface Temperature product [OISST v2, available from NOAA/OAR/ESRL PSD, Boulder, Colorado, USA, at https://www.esrl.noaa.gov/psd/; *Reynolds et al.*, 2007; *Reynolds*, 2009]. For sea ice concentration, we used the AMSR-2 derived dataset provided by the Institute of Environmental Physics, University of Bremen, Germany [*Spreen et al.*, 2008]. Surface wind fields (10 m above sea level), sea level pressure, surface air temperature (2 m above sea level), as well as air-sea heat and radiative fluxes were extracted from ERA Interim [*Dee et al.*, 2011]. ERA Interim has a horizontal resolution of $0.75° \times 0.75°$, which for the study region at 80-82° N corresponds to a much higher resolution in the zonal direction (10.9-14.1 km) as compared to the meridional direction (83.3 km). To obtain values at the mooring locations, data were bilinearly interpolated from the respective nearest grid points onto the moorings positions.

### 2.3 Heat content change derivation

To assess heat content changes in the upper ocean, we combined SST and temperature observations from the moorings using linear interpolation to fill the gap between the SST record and the uppermost temperature sensor on the moorings. While the resulting interpolated profile will not capture the full variability in the water column, comparison with CTD casts during deployment and recovery shows that moored and shipboard CTD profiles are comparable without systematic bias. *Reynolds et al.* [2007] give a total error estimate for the derived SST in their Figure 8, which shows a deviation of up to 0.5° C in our study region. A main source of uncertainty in the OISST v2 product is the simulation of SST in the presence of sea ice which might lead to a negative bias when ice concentration are higher than 75% and positive bias for concentrations between 50 and 75%. See Supporting Information and Figure S1 for more details and discussion. We then calculated daily mean temperature ($T$) and density ($\rho$; using average salinity from the mooring sensors) of the upper 200 m water column. Heat content ($Q$) per cubic meter of the upper 200 m was then calculated as follows:

$$Q = \rho \cdot V \cdot C_p \cdot T \tag{1}$$

with $V = 200\,\mathrm{m}^3$ for the entire volume, and $C_p$ = specific heat of seawater. We used temperatures in [° C] which is equivalent to using a reference temperature of 0° C. Heat content change $dQ$ is calculated according to

$$dQ = \Delta Q/\Delta t \tag{2}$$

with $t$ = time step.

### 2.4 Vertical mixing inferred from internal wave-based parameterisation

During autumn and early winter, when the 800-m mooring at 31° E was frequently blown down due to strong currents and thus "profiled" the water column, the two uppermost CTDs provided temperature and salinity data from a depth range of 20 to 60 m. Combining the hydrographic data with ADCP current shear variance in an internal-wave-based parameterisation yields estimates of vertical mixing (Henyey-Wright-Flatte scaling [*Henyey et al.*, 1986], using the same scaling and reference values as in *Wijesekera et al.* [1993]). Dissipation of turbulent kinetic energy, $\varepsilon$ at time $t$, can be estimated as:

$$\varepsilon(t) = \frac{1.67}{\pi}(bN_0)^{-2} f \cosh^{-1}\left(\frac{N}{f}\right) j_*^2 E_{meas}(t)^2 \tag{3}$$

where scaling depth $b = 1300$ m, reference buoyancy frequency $N_0 = 3$ cph, and vertical mode scale number $j_* = 3$. $E_{meas}$ is estimated as $(\Phi_{uu} + \Phi_{yy})/2$, where $\Phi_{uu,yy}$ are power density spectra of 20 day records of horizontal velocity ($u$, $v$) at individual depths, integrated between $f$ (Coriolis frequency) and 1 cph. The CTD data are differenced over 8 m intervals to provide values for $N^2$.

Vertical diffusivity, $K$, can then be found using

$$K = \Gamma\varepsilon/N^2 \tag{4}$$

[*Osborn*, 1980], applying the canonical factor $\Gamma = 0.2$. Combining this with observed vertical temperature gradients, the vertical heat flux, $F_H$, can be calculated as

$$F_H = -\rho_0 C_p K dT/dz \tag{5}$$

where $\rho_0 = 1027\,\mathrm{kg/m}^3$ is the density of seawater, and $C_p$ is the specific heat of seawater.

The above calculations will capture not only effects of internal waves but also of wind-driven shear in the upper ocean. It should also be noted that density gradients can be weak in autumn resulting in large uncertainty for diffusivity and heat flux values (see Eq. 4). A previous analysis based on the same method to calculate dissipation and diffusivity using a subset of this data set, applied the results to estimate the vertical redistribution of nutrients to assess the development of the *in situ* nitrate pool [*Randelhoff et al.*, 2015]. Their results support the levels of diffusivities presented here.

### 2.5 Ekman pumping and associated upwelling

Surface wind stress for the study region was calculated with

$$\boldsymbol{\tau} = (\tau_x, \tau_y) = \rho_a C_d U_{10} \mathbf{U}_{10} \tag{6}$$

with air density $\rho_a = 1.25\,\mathrm{kg\,m^{-3}}$, zonal wind speed $U_{10}$ and wind vector $\mathbf{U}_{10}$ at 10 m above sea level, and using the lower threshold value for the mean air-ocean and air-ice drag coefficient $C_d = 2.7 \cdot 10^{-3}$ for outer marginal ice zones ( 50% ice concentration) [*Guest et al.*, 1995; *Lind and Ingvaldsen*, 2012]. With this approach, we assume that all the momentum in the ice is transferred to the ocean. Daily values of Ekman pumping were calculated using

$$w_e = \frac{1}{\rho_w f}\left(\frac{\partial \tau_y}{\partial x} - \frac{\partial \tau_x}{\partial y}\right) \tag{7}$$

where $\rho_w$ is the mean ocean mixed layer density (taken as $1025\,\mathrm{kg\,m^{-3}}$) and $f = 2\Omega \sin\varphi$ is the Coriolis acceleration at latitude $\varphi$. $\tau_x$ and $\tau_y$ were set to 0 on land. For time series of Ekman pumping at the mooring locations, gridded Ekman pumping was bilinearly interpolated onto the mooring positions.

## 3 Results

### 3.1 Hydrographic variability of the boundary current over the continental slope north of Svalbard and its impact on the sea ice cover

Both the hydrography and sea ice cover vary considerably during the course of the one-year deployment period (Fig. 2). The mooring sites at 200 m and 800 m are ice-free in summer and autumn 2012 (Fig. 2 b). In November, a patch of sea ice is advected from the north as can be seen from satellite observations [not shown; *Tschudi et al.*, 2016, accessed 29 May 2018], but disappears again completely at the end of the month. The ice only returns in late January, but the sea ice concentration decreases again in the second half of February, after which the ice cover remains dense until complete melt in July. The presence and persistence of sea ice is strongly reflected in the SST (Fig. 2 c). After high temperatures in autumn 2012, SST was temporarily reduced when sea ice drifted into the study region in mid-November. Following this, the SST increased again, which contributed to ice melt despite air temperatures remaining low ($< -9^\circ$ C; Fig. 2 b). The temporary decrease in ice concentration in February occurs concurrently with elevated SST. During periods of dense ice cover (March-June), temperatures in the upper ocean (0-50 m) are markedly reduced. Low temperatures remained in the sub-surface layer even after surface temperatures increased due to heating by solar radiation in late June.

In autumn, the core of the AW boundary current is situated close to the 800 m isobath [see Figures 3 and 7 in *Våge et al.*, 2016; *Pérez-Hernández et al.*, 2017, respectively]. The variability captured by the 800 m mooring should therefore be representative of the variability in the main part of the boundary current during autumn. Information about potential shoaling or deepening of the boundary current during other seasons is lacking, and the mooring time series might be less representative of the boundary current core outside autumn. In the time series from the 800 m mooring, the AW core with the highest temperatures and highest salinities is generally located between 100 and 500 m depth (Fig. 2 c; for time series of salinity see Fig. S1 b). There is significant variability in both the vertical extent of the AW layer as well as its temperature and salinity throughout the year.

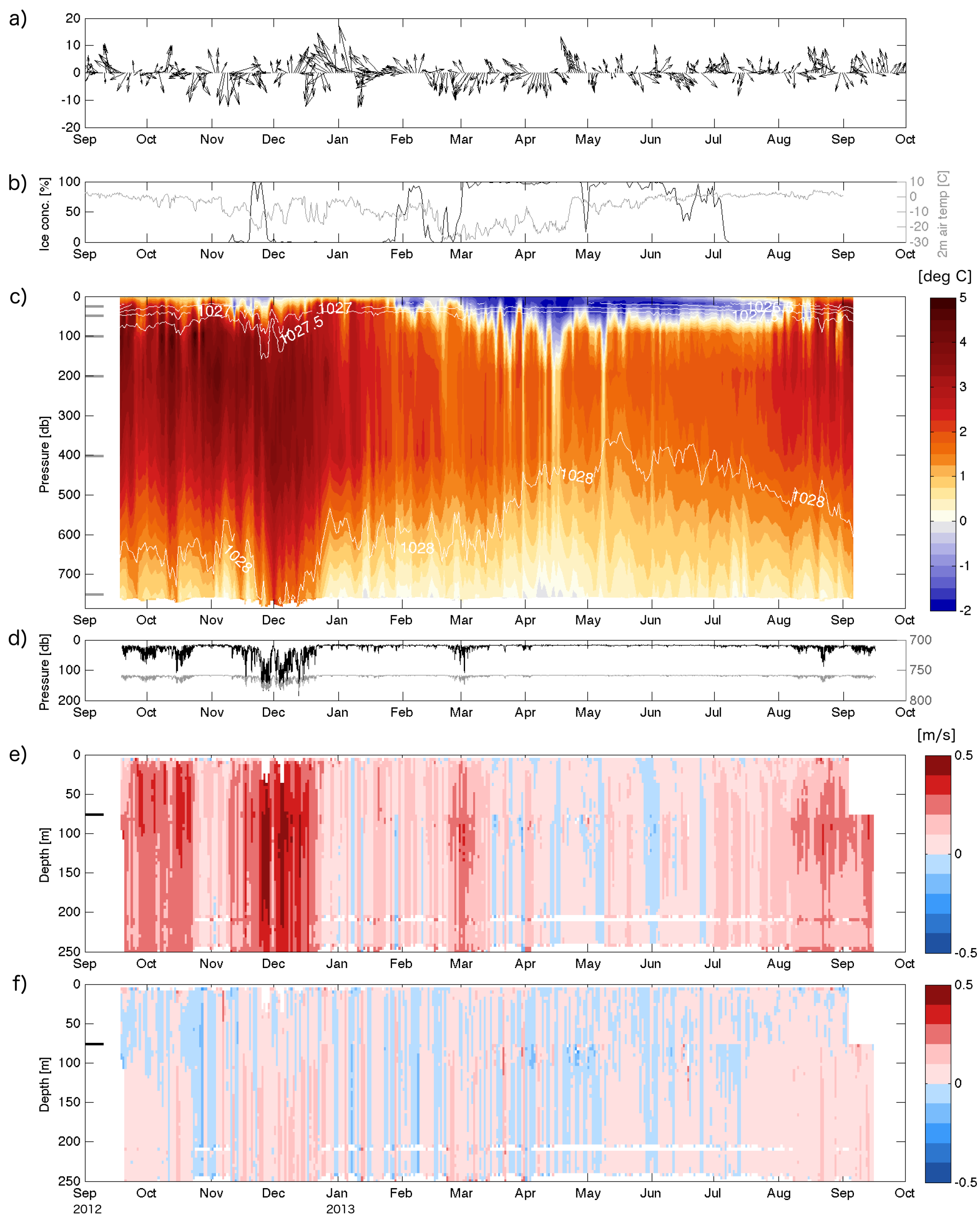

**Figure 2.** Time series at the 800 m mooring site. a) Daily wind vectors at 10 m above sea level. b) Sea ice concentrations and 2 m air temperature. c) Daily averaged potential temperature from SST and CTD sensors on the mooring. The white contour lines show density. Grey markers on the left y-axis indicate average sensor depth. d) Daily pressure from top (black, left-hand y-axis) and bottom (grey, right-hand y-axis) CTD sensors. e) Daily averaged along-slope current from the combined ADCP record. The black marker on the y-axis shows where the ADCP records were joined. f) Same as e) except for the across-slope current.

The warmest and most saline water is observed in autumn and early winter (September-January), when $T > 3°$ C and $S > 35$, during which time the vertical extent of the AW layer is largest. Both $T$ and $S$ decrease during late winter and remain low during spring and early summer. A similar situation can be seen at the 200 m mooring on the shelf (Figs. S1 and S2) with warm and saline water in autumn and early winter, and the onset of cooling at the surface with progression down into the water column in late winter to spring.

The circulation in the study area is generally dominated by the along-slope flow of AW (Fig. 2 e & f). The currents are strongest in autumn and weaker in spring and early summer. A marked event occurred in late November/early December, with currents strong enough to blow down the 800 m mooring as visible from the pressure records in Fig. 2 d. These enhanced currents in the AW layer led to an increased presence of warm, saline water, which was followed by the disappearance of the sea ice that had been previously advected into the region, and an increase in SST. The current meter time series at 402 m and 754 m (not shown) confirm that velocities are elevated throughout the water column. This is concurrent with higher temperatures and salinities also at depth, suggesting an increase in the vertical extent of the AW layer at the 800 m mooring. The velocities at 402 m generally follow the same pattern of variability as recorded by the shallower ADCPs. The lowest current meter, situated roughly 100 m above the sea floor, shows the same pulses of strong currents during autumn and winter, but higher velocities from March onwards during the ice-covered period. The stronger velocities in late November/early December are also recorded on the shelf, albeit to a lesser degree (Fig. S2). The 200 m mooring also shows similar elevated temperatures and salinities along with a temporary decrease in density in November/December.

Various processes such as heat exchange with the atmosphere, and wind- or tide-induced mixing can influence the upper ocean heat content north of Svalbard. In the following sections, we begin by investigating heat content changes of the water as it progresses from the upstream mooring at 22° E to the main mooring line at 31° E (for temperature recorded at the upstream mooring see Fig. S3). While advection is likely the largest contributor to the local heat content variability, local processes can lead to significant vertical fluxes which influence the heat budget. After an initial look into heat exchange at the ocean-atmosphere interface, we investigate the role of vertical fluxes in the water column as deduced from current shear variance as well as the influence of tides. While wind-driven upwelling is a well documented process in parts of the Canadian Arctic [e.g. *Pickart et al.*, 2013], the shelf geometry north of Svalbard is not favourable for shelf-break upwelling driven by along-slope winds [*Randelhoff and Sundfjord*, 2018]. We show, however, that Ekman pumping can lead to instances with considerable isopycnal uplift. To fill in the 3D-picture of processes affecting the heat content at our main mooring site, we also discuss the potential role of eddies for cross-slope redistribution of heat.

### 3.2 Heat content and along-slope heat loss in the boundary current

Heat content in the upper 200 m, i.e. from the core of the Atlantic Water layer to the surface, experiences a seasonal cycle with highest values in autumn and a minimum in spring (Fig. 3 a). As expected, heat content is higher at 22° E than at 31° E as heat is lost during the eastward transit. Over the entire deployment period, the upper ocean heat content difference between the two moorings is $4.8 \cdot 10^8\,\mathrm{Jm^{-3}}$, which amounts to a heat loss of $16.7\,\mathrm{Wm^{-2}}$ over the 145 km distance. Fig. 3 b) and c) show heat content change in the upper 200 m at the upstream and the main 800 m mooring on short (daily) and longer (20-day averaged) temporal scales, respectively. While there is considerable variability throughout the mooring record, changes are largest during autumn and spring, whereas the late winter period and especially the summer period are more stable. The seasonal cycle during our study period is similar at both locations; however, some differences exist. Changes in heat content at the western mooring often show up after a delay of several

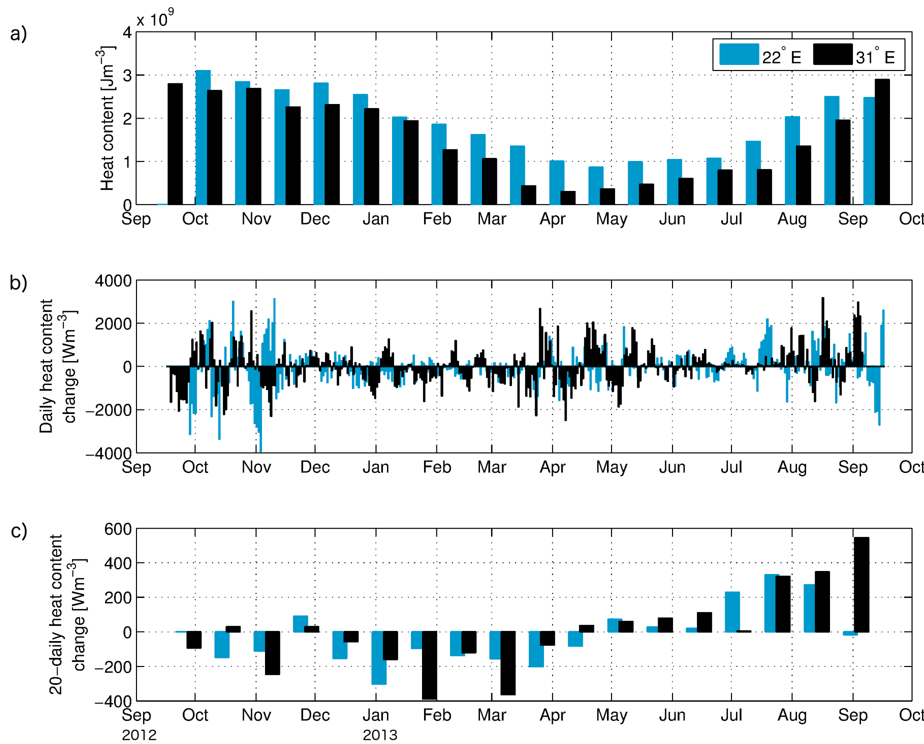


312 **Figure 3.** a) 20-day average of heat content in the upper 200 m water column at both 800 m moorings relative to 0° C. b) Seven-day running average of daily heat content change for the upper 200 m at the 800 m moorings at 22 and 31° E. c) 20-day average heat content change.

days to weeks at the eastern mooring, demonstrating the importance of advection in the region. Nevertheless, changes occur at 31° E that are not recorded at the western mooring first (and vice versa), indicating the importance of local processes for redistribution of heat. Covariance analysis using lagged correlations confirms that over 80% of the variability in the 20-day heat content change at 31° E is driven by changes upstream, whereas changes on daily to weekly time scales are dominated by local processes.

The travel time between the moorings at 22° E and 31° E can be assessed through the correlation between the (daily averaged) 50-m temperature records at the upstream mooring and the main 800 m mooring. For the entire time series the maximum correlation (0.78) corresponds to a five day time lag between the two sites. A similar lag is found for all seasons. Correlation analyses for shorter periods (order 100 days) give lower values than the whole time series, which indicates that the seasonal signal in temperature might increase the full-length correlation value. For late winter, when the temperature signals are weaker and upper-column stratification reduced, the time lag found through correlation analysis might also reflect bias from surface processes occurring more or less simultaneously at both locations. We thus expect that the true travel time is longer when the currents are weaker in spring and summer.

The ADCP data from 31° E yield a deployment mean along-slope current speed of 0.12 $\mathrm{ms^{-1}}$ at 50 m depth with strong seasonality: in the autumn (until 21 December) the mean speed is 0.24 $\mathrm{ms^{-1}}$ compared to 0.09 $\mathrm{ms^{-1}}$ for the remaining period. The mean travel time based on these values thus varies between one week in autumn to nearly three weeks in spring. We therefore choose a two week lag to calculate the difference in weekly mean temperatures at the two moorings as shown in Fig. 4 c). The temperature at 50 m depth between the upstream 800 m mooring at 22° E and the 800 m mooring in the main array at 31° E is shown in Fig. 4 b). The upstream water is considerably warmer most of the time, typically by as much as 1–2° C (see also SFig 3).

The strong event with increased currents in late November/early December recorded at the main 800 m mooring does not show up clearly in the daily heat content changes (Fig. 3 b). However, the 20-day averages display a jump from negative to positive heat content change, i.e. a heat gain in the upper ocean (Fig. 3 c). This difference between the daily and the 20-day averages indicates the different timescales involved regarding advective or local signals (Fig. 3 a) which possibly are caused by local differences in ice coverage leading to both direct and indirect effects (e.g. limiting direct air-sea heat exchange, and/or changing surface stratification and thus mixing and vertical fluxes). As cooling from the surface sets in later in winter, combined with reduced temperatures and salinities in lower layers, the heat content is steadily lowered from January until late March, when the upper ocean starts gaining heat again. Shortly after this, in late April, an opening in the ice pack occurs followed by strong short-term heat loss. From the end of July, heat content changes are mostly positive and the upper ocean heat content increases throughout the summer into autumn.

Assuming uniform heat loss at 50 m depth along the 800 m isobath in the study area, the magnitude of the loss can be estimated from the temperature difference between the two mooring sites as shown in Fig. 4 c). Again, seasonality is strong. We estimate mean values of 36 $\mathrm{Wm^{-2}}$ for autumn and early winter (September-March) and 15 $\mathrm{Wm^{-2}}$ for spring and summer (April-September). Two month-long periods in October-November and February-March have mean heat loss estimates $> 50\,\mathrm{Wm^{-2}}$. These values, which are associated with periods of elevated heat loss, are significantly higher than the estimate based on the 0-200 m heat content difference between the two moorings. This suggests that losses are enhanced near the surface, whereas the AW layer retains most of its heat.

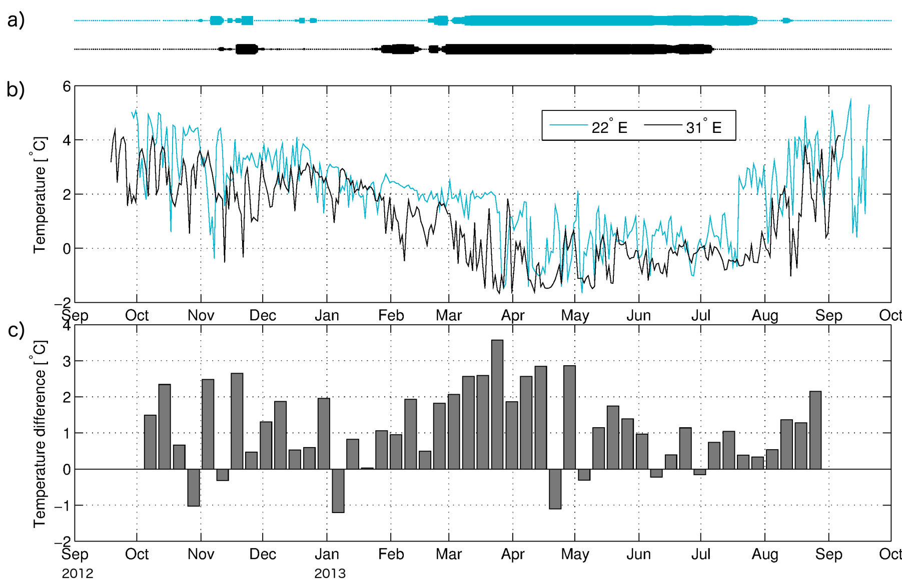


**Figure 4.** a) Ice coverage at 22 (blue) and 31° E (black). The thickness of the bars indicates ice concentration between 0 (thinnest) and 100% (thickest). b) Daily averaged temperature at 50 m at 22 and 31° E. c) Difference (22° E - 31° E) of weekly means with a two week lag to account for the passage of the 145 km distance between the moorings.

## 3.3 Vertical heat flux at 31° E

### *3.3.1 Air-sea heat fluxes*

Heat fluxes at the air-sea interface vary with season and are influenced by the presence of sea ice. Incoming shortwave radiation is only available from mid-March to mid-September when the sun rises above the horizon. Temperature gradients between the ocean and the atmosphere are largest during winter, leading to high oceanic sensible heat loss in the absence of consolidated sea ice. The arrival of sea ice strongly decreases sensible and latent heat loss and hence reduces the heat flux variability in late winter and spring (Fig. 5). During September to March, the ocean loses on average over 200 $\mathrm{Wm^{-2}}$ heat to the atmosphere, whereas in March to August, it gains around 80 $\mathrm{Wm^{-2}}$ (Fig. 5). Several notable heat flux events occur during autumn and winter, when over periods of five days to two weeks, heat loss exceeds 400 $\mathrm{Wm^{-2}}$. Intermittent periods with weak heat fluxes are connected to the presence of sea ice inhibiting exchange between the ocean and the atmosphere, which is most pronounced in the first half of February (Figs. 2 b) and 5). For a one-week period (4-10 Feb), ice concentrations are high following a period with easterly to southerly winds and air temperatures of -5 to -15° C (Fig. 2 a and b). During that time, the average oceanic heat loss to the atmosphere is about 58 $\mathrm{Wm^{-2}}$. The three week period that follows is characterised by predominantly northerly winds which disperse the ice pack and advect cold air masses, lowering air temperatures to nearly -30° C. The large temperature gradient between the air and the open water lead to an average ocean heat loss of 331 $\mathrm{Wm^{-2}}$ during 11 Feb - 01 March. Between March and July, the region remained ice covered with strongly reduced air-sea fluxes of $\sim$9 $\mathrm{Wm^{-2}}$. The variability observed in the air-sea heat flux is not directly reflected in the ocean heat content at the 800 m mooring (Fig. 3).

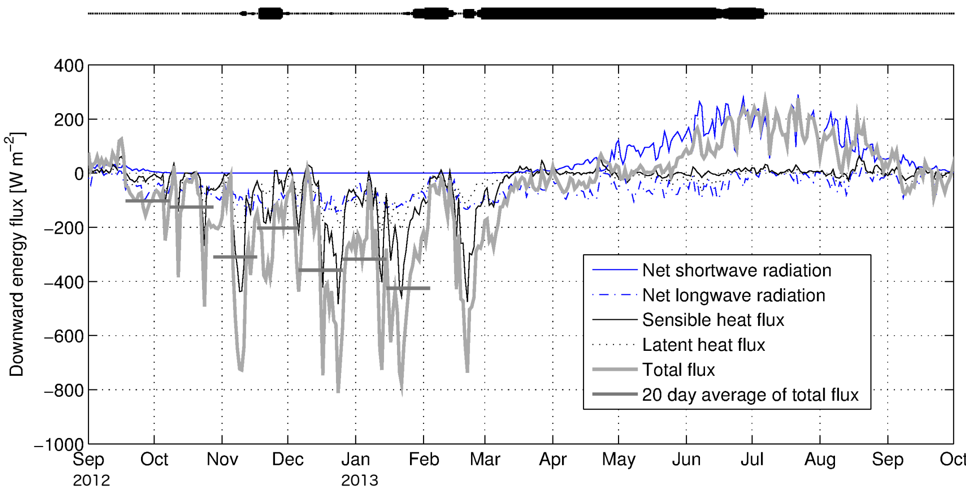


**Figure 5.** Energy budget at the ocean - atmosphere interface from ERA Interim data [*Dee et al.*, 2011] at the main 800 m mooring location. Positive = downward flux (ie. from atmosphere to ocean), negative = upward flux. Total flux is the sum of short- and longwave radiation and sensible and latent heat flux. The bar at the top indicates presence of sea ice at the main 800 m mooring; see also Fig. 4.

#### *3.3.2 Vertical heat flux estimate from shear variance and hydrography*

Dissipation in the upper water column (from current shear and stratification profiles, see Section 2.4) is periodically enhanced ($> 10^{-8}$ W kg$^{-1}$) in autumn and early winter. Highest values are typically found above 30 m (Fig. 6, left panel) and correspond to strong wind events (Fig. 2 a). Lower dissipation coincides with high sea ice concentrations (e.g. November to early December), when sea ice possibly reduces the transfer of wind energy and introduces a melt water layer, restricting the depth range of wind-driven mixing. In late January, sea ice concentrations were low, but potential ice melt could introduce melt water, which increases the stability in the surface layer above our measurements. Nevertheless, dissipation in the 20-30 m interval is enhanced compared with dissipation in deeper layers, and is larger than during the late November period of high ice concentrations.

Heat fluxes exceeding 100 Wm$^{-2}$ are seen in the 20-30 m interval, while the heat flux is typically around 20-50 Wm$^{-2}$ at 50 m depth (Fig. 6, right panel). These estimates compare well with the independent calculations of along-slope heat loss over the 800 m isobath for autumn 2012, where 20-day means at 50 m depth were around 30 Wm$^{-2}$ (see Section 3.2). The periods of strong heat flux correspond with the periods of strong dissipation, with the exception of late September to early October when mixing was moderately enhanced but the heat flux did not exceed 50 Wm$^{-2}$. During this time the stratification was strong and the temperature gradient modest in the 20-30 m depth range.

Air-sea fluxes averaged over the same periods as dissipation and upper ocean vertical heat flux vary in similar fashion, particularly in the absence of sea ice (Fig. 5). In general, air-sea fluxes are higher than the sub-surface heat flux. This is to be expected as long as there is a temperature gradient in the water column, since wind-induced vertical mixing typically decreases from the uppermost part of the water column to the 20-30 m depth interval and below. If near-surface lateral heat resupply is not sufficient to maintain the heat content, excessive surface hat loss will cool the upper part of the water column over time.

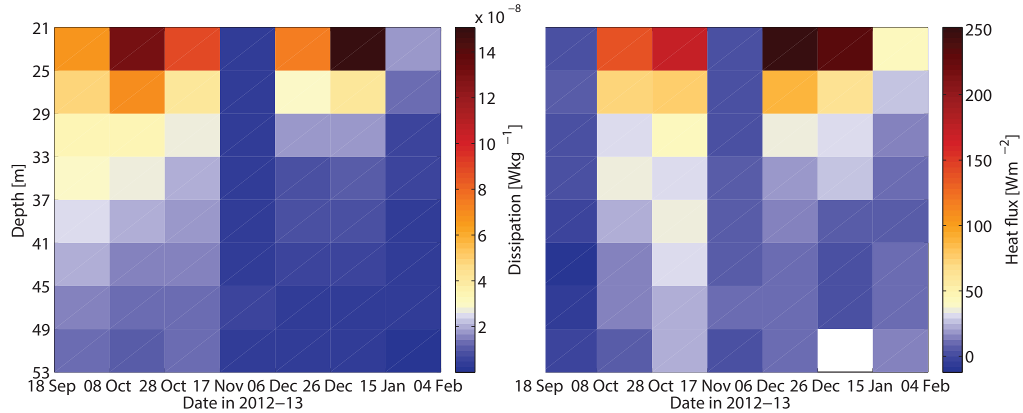


**Figure 6.** 20-day averages of TKE dissipation (left panel) and vertical heat flux (right) from ADCP current shear variance, stratification and temperature gradient from the upper part of water column for the autumn-early winter period when the 800 m mooring was being blown down frequently. The white field in the lower layer in late December-early January is due to lack of CTD data in that period.

During 17 Nov - 06 Dec, the period with a strong wind event and an average sea ice concentration of 35%, heat loss to the atmosphere is lower than in the ice-free periods before and after. The sub-surface vertical mixing and heat flux are also reduced during this period, possibly the result of strengthened stratification due to freshening of the near-surface layer. The largest difference between surface and water column fluxes occurs in late January (15 Jan - 04 Feb). Then, air-sea heat loss reaches its maximum, while heat flux in the upper ocean is significantly reduced. During this period, the ice cover is building up again, but average concentrations are still quite low (16%). Air temperatures are comparable to the autumn period with reduced upper ocean vertical heat flux, and both periods have average winds in excess of 5 $\mathrm{ms^{-1}}$. The major differences lie in the ocean: freshwater is introduced from melting sea ice, hampering vertical mixing, and temperature in the sub-surface layer has started to decrease (Fig. 2 c). Thus, less heat is available and the temperature gradient in the upper several tens of meters is reduced, potentially as a result of the continuously large air-sea heat loss. During the ensuing weeks, air-sea fluxes are also strongly reduced, until more upper-ocean heat becomes available again in late February (Fig. 2).

#### *3.3.3 Effect of tides on mixing*

Tides are comparatively weak over the deep Arctic Basins, but can be considerable in certain continental slope and shelf regions of the Barents, Kara, and Laptev Seas [*Padman and Erofeeva*, 2003]. Tides are known to interact with irregular topography along the slopes and shelves to promote vertical mixing through breaking internal tides and shear instabilities [*Rippeth et al.*, 2015]. Near the $M_2$-critical latitude (~75° N), tides were shown to be strongly dependent on stratification and lead to shear instabilities and enhanced turbulent dissipation [*Lenn et al.*, 2011; *Janout and Lenn*, 2014]. Considering the importance of turbulence and dissipation for vertical fluxes, we next investigate the dominant frequencies that control the dynamics above the north Svalbard continental slope by performing a rotary spectral analysis [*Gonella*, 1972] on the vertical shear records at both the 200 m and 800 m mooring locations. Shear as well as current (not shown) spectra at both locations are dominated by clockwise rotating semidiurnal frequencies, in particular the $M_2$-tide (Fig. 7). The spectra underline that tides are much more energetic at the shelf break (200 m mooring) compared with the deeper slope. The record also resolves several $M_2$-

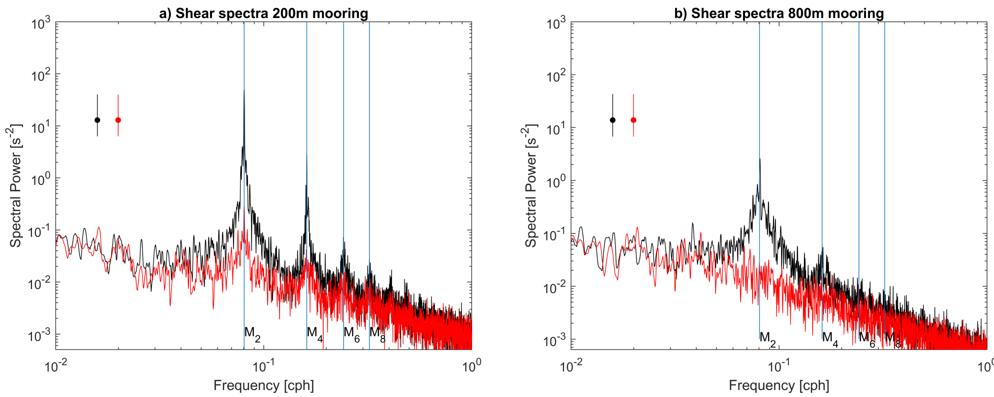


**Figure 7.** a) Clockwise (black) and counterclockwise (red) rotating component from rotary spectra analyses [*Gonella*, 1972] of vertical shear (i.e. the vertical difference in current velocity between 20 m and 100 m. The analyses were performed on the 200 m (left) and 800 m (right) mooring ADCP records. The inset vertical lines indicate the confidence interval. The frequency of the $M_2$-tide and its overtides ($M_4$, $M_6$, $M_8$) are indicated by the thin blue vertical lines.

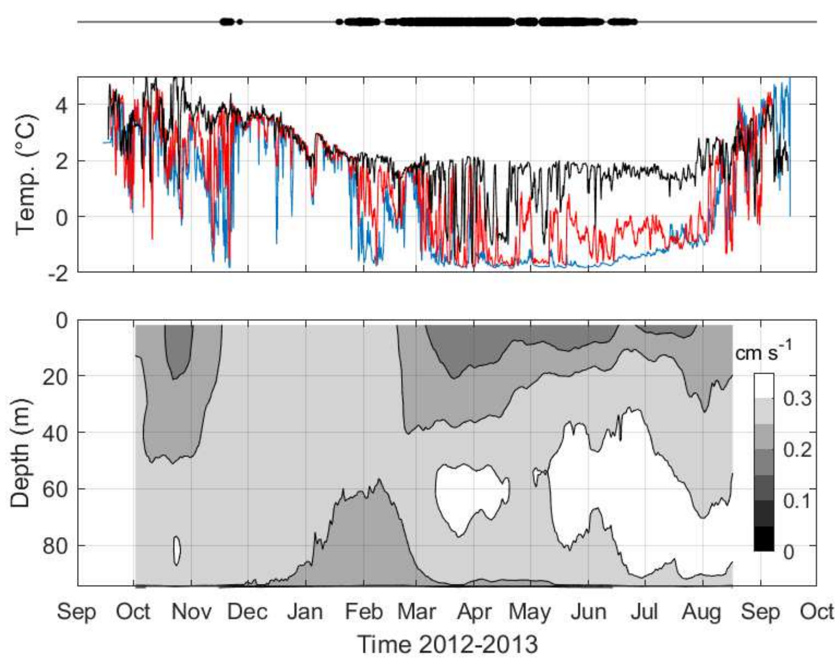


**Figure 8.** Top) sea ice concentration (as in Fig. 4); middle) temperature at 20 m (blue), 40 m (red), and 100 m (black); bottom) major axis of the $M_2$ (cm s$^{-1}$) throughout the year-long deployment.

overtides ($M_4$, $M_6$, $M_8$) in both currents (not shown) and shear spectra (Fig.7), which points to nonlinear interaction of the $M_2$-tide with the bottom topography at the 200 m mooring location with potential relevance for mixing as well. This is further underlined in an amplification of the counterclockwise component, which is not the case at the deeper location.

Harmonic analysis using the Matlab T-Tide package [*Pawlowicz et al.*, 2002] was performed on the current records to extract the relevant tidal constituents, with focus on the dominant $M_2$-constituent and their parameters. In order to assess the seasonal variability of the tidal structure, we performed 30-day overlapping tidal analyses for the 200 m mooring's current record in the upper 100 m (Fig. 8). The $M_2$ tides appear to be impacted by the sea ice cover as well as by stratification. While the tides are more homogeneous during early winter when sea ice was still absent, a sub-surface maximum at 60 m occurs as soon as the region is ice-covered (February-August). This sub-surface tidal maximum generally coincides with the presumed depth of the pycnocline [*Janout and Lenn*, 2014]. While CTD records from above 100 m are unfortunately not available from the 200 m mooring (Table 1), the seasonal progression of the top 100 m hydrography can be derived from the 800 m mooring record. As previously described, the 100 m temperatures are relatively stable (2-4° C) compared to 20 m and 40 m (between near-freezing to > 4° C). After reaching a maximum in late autumn, coincident with the strong along-slope flow (Fig 2), temperatures are relatively homogeneous in the upper 100 m until February; also a period where the tidal structure is largely homogeneous. Beginning in February 2013, sea ice is present and the 20 m-temperatures become highly variable due to mixing and cooling and finally arrives at the freezing point, which implies that a winter pycnocline is established somewhere between 20 and 100 m. This pycnocline persists until August 2013, after the sea ice disappeared.

Acoustically profiled currents and the tidal structure can provide useful information regarding stratification in ice-covered regions in the absence of upper layer instruments [*Janout et al.*, 2016]. Considering that stratification generally suppresses turbulence and hence vertical mixing, enhanced tidal shear at the pycnocline thus presents a mechanism to counteract this suppression and contribute to diapycnal mixing between the 2° C warm water at 100 m and the near-freezing surface waters. The considerable semidiurnal tidal currents and shear are especially relevant at the shelf break and are likely a source of energy and dissipation and hence important for vertical mixing there, as supported by observations [*Rippeth et al.*, 2015] and models [*Luneva et al.*, 2015]. Moored (ice track-capable ADCP) ice drift measurements generally show semidiurnal oscillations in a mobile ice cover in other regions where tides are important [*Janout and Lenn*, 2014]. The decreasing role of tides manifested in the shear spectra between our 200 m and 800 m moorings (Fig. 7) implies that surface currents and hence the ice cover above the continental slope diverges twice-daily. The likely consequence is enhanced lead openings and increased air-sea fluxes, which underlines the need for further studies on the effect of tides for the regional heat budget.

### 3.4 Wind-driven vertical transports

Several studies have demonstrated the importance of vertical fluxes associated with wind-driven shelf-break upwelling in the Canadian Basin of the Arctic Ocean [e.g. *Carmack and Chapman*, 2003; *Pickart et al.*, 2009; *Schulze and Pickart*, 2012]. The shelf north of Svalbard is 150 - 200 m deep, versus 50 - 60 m in the Beaufort Sea where upwelling is particularly common. The much greater depth north of Svalbard implies that shelf-break upwelling is not likely to be important here; the outer shelf is too deep for the surface and Ekman layers to overlap and interact [see *Randelhoff and Sundfjord*, 2018]. In addition, the wind field is highly variable both in strength and direction with only few short periods of easterly (i.e. upwelling favourable) winds lasting several consecutive days (Fig. 2 a). Using the same approach as *Lin et al.* [2018] applied to detect upwelling events in the Beaufort Sea , we were not able to identify similar events at our shelf break mooring location (200 m bottom depth) related to the wind forcing (Fig. S4). Furthermore, assuming that shelf break upwelling should lead to isopycnal tilting, we compared the density at both 100 and 200 m from our two moorings with density from a mooring concurrently deployed 10 km farther offshore near the 2100 m isobath (*Perez-Hernandez, in prep.*). No events of density difference change in response to upwelling favourable winds were detected.

Independent of the coast and shelf geometry, upward and downward Ekman pumping due to divergent or convergent wind stress can contribute to vertical transport of water and thus heat. Fig. 9 shows seasonal averages of wind stress and wind stress curl over the broader region for the period September 2012-August 2013. In general, positive wind stress curl, supporting upward pumping, prevails at the mooring sites. During winter, both Ekman transport and pumping are variable with strong episodes of varying directions (Fig. 10 a and b). The largest negative pumping events take place in autumn and early winter, but positive Ekman pumping dominates. Over the period Sep 2012 - Aug 2013, we estimate an overall net upward pumping of on average 8.7 cm day$^{-1}$. After a short period of overall negative pumping in November with a suppression by over 6 m, several strong positive episodes occur in December and January with $>$ 200 cm day$^{-1}$ vertical movement. The average pumping for 15 December 2012 to 14 January 2013 is 65.1 cm day$^{-1}$, which results in an accumulated uplift of 19.5 m in that period (Fig. 10). In March - May, theoretical Ekman pumping is modest with on average 6.5 cm day$^{-1}$. In this period, sea ice concentrations are near 100%, and transfer of wind stress to the ocean and thus Ekman transport is reduced. In the ice-free summer season from mid-July, Ekman pumping is around 4.6 cm day$^{-1}$.

To detect Ekman pumping in the mooring record, we extracted a time series of average wind stress curl at the 200 m and 800 m mooring location on the main array and attempted to match events of large wind stress curl (positive or negative) with changes in density. At the 200 m mooring, we used density directly from the CTD sensors situated at 104, 131, and 180 m depth. We do not find any clear pattern in the mooring record that could consistently be associated with strong wind events. Only the very large uplifts derived from wind stress curl in late December and early January can be matched with increasing density. At the 800 m mooring, the water column is too weakly stratified for a signal to be detected in either density records from the CTD sensors or the interpolated time series.

### 3.5 Cross-slope redistribution of heat

Part of the along-slope heat loss will be lateral, including slope-shelf exchange and a portion of the flow turning south into the Kvitøya Trough [*Pérez-Hernández et al.*, 2017]. We assume that the major part of the advective loss to the shelf and the trough occurs from the up-slope part of the boundary current and does not affect the heat content over the 800 m mooring. Basin-ward losses, and in particular shedding of mesoscale eddies, can potentially be a larger sink for the central and outer part of the boundary current. During the 2012 A-TWAIN cruise, warm-core anticyclonic eddies were observed over the deeper part of the slope [*Våge et al.*, 2016]. In 2013, a cyclonic eddy was detected [*Pérez-Hernández et al.*, 2017]. As boundary current eddies often form in dipole pairs, the cruise-based observations suggest that warm-core eddy shedding occurs at least intermittently in this area. A numerical study, analysing simulations from an eddy-resolving model (ROMS, horizontal resolution 800 x 800 m, see *Crews et al.* [2018]) from the slope area north of Svalbard, identifies and tracks numerous eddies forming there. In that study, the area east of 20° E appears to be particularly important with respect to shedding eddies that actually emanates from the boundary current and travel into the deep basin. On average, around one eddy per week leaves the boundary current in that area, but only a few of these will actually cross our main mooring array. Conservative estimates of the vol-

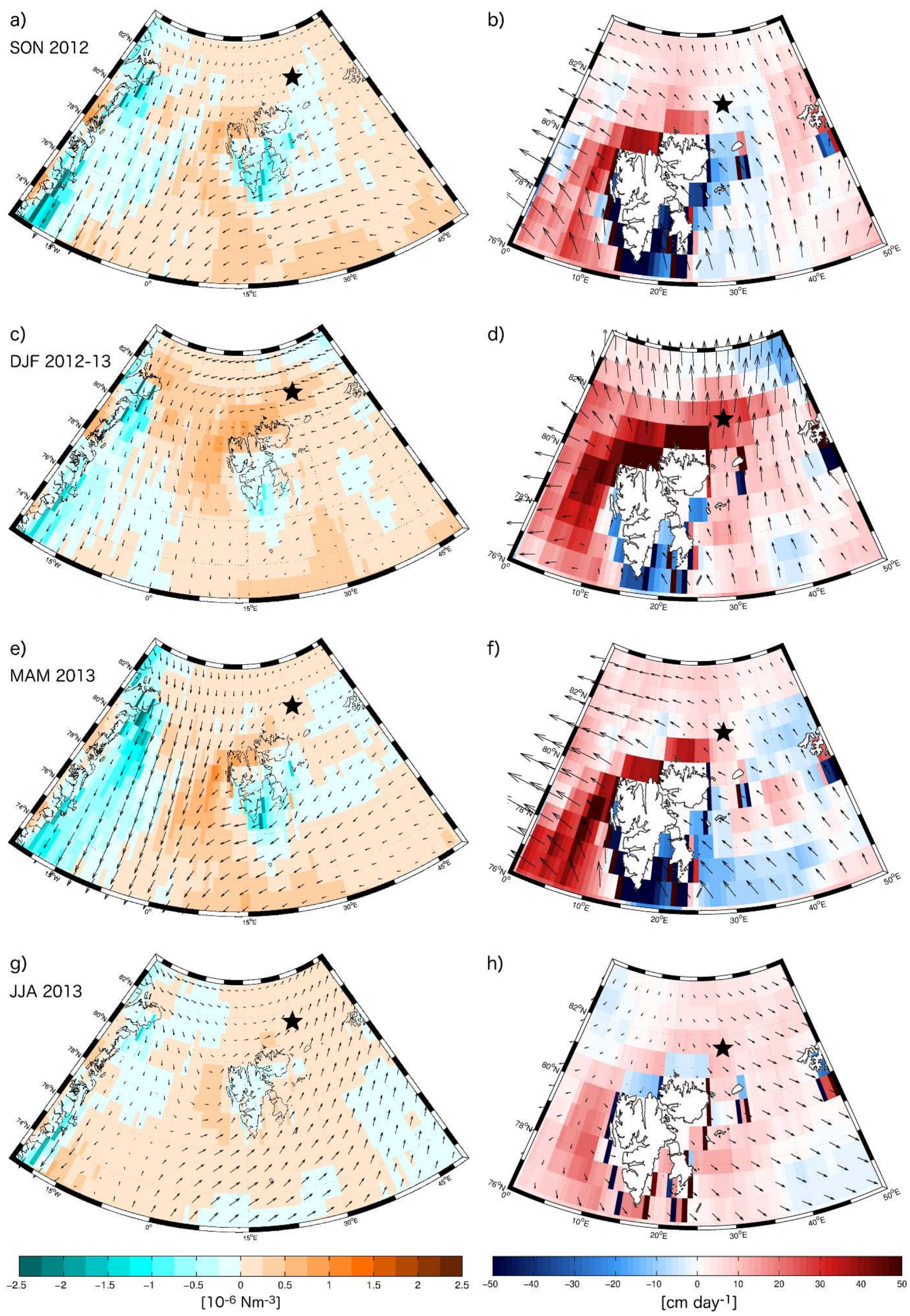


**Figure 9.** Seasonal averages of wind stress (arrows; every 4th data points along the longitudinal axis) and wind stress curl (background colour) on the left, Ekman transport (arrows; every 4th data point along the longitudinal axis) and Ekman pumping (background colour; positive values are upwards) on the right. a) and b) September-November 2012; c) and d) December 2012-February 2013; e) and f) March-May 2013; g) and h) June-August 2013. The location of the main mooring line is indicated by the black star.

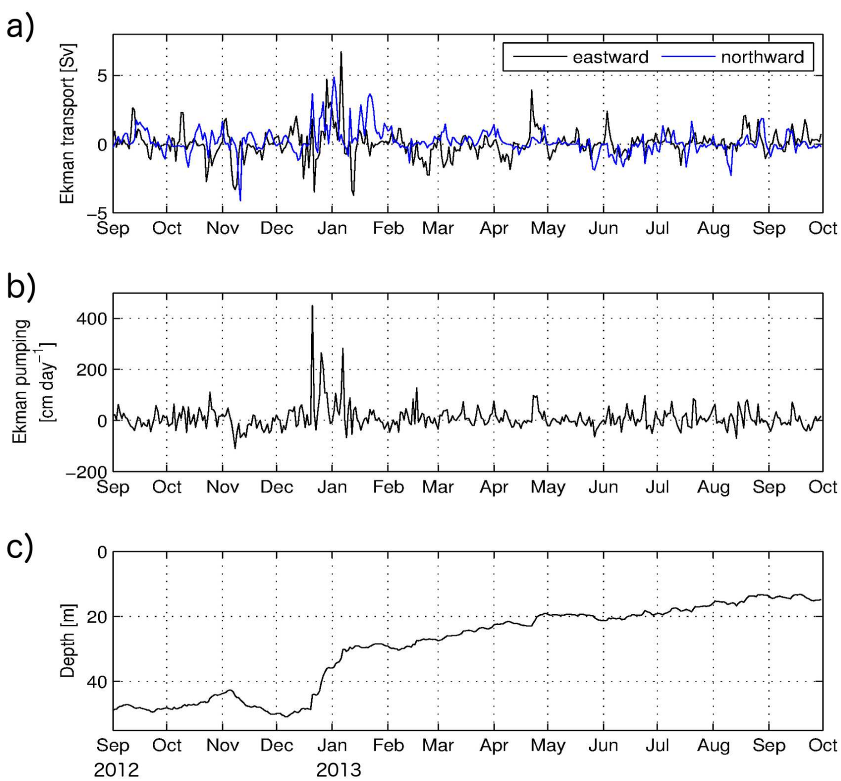


**Figure 10.** a) Daily average Ekman transport resulting from local wind stress at the 800 m mooring. b) Rate of resulting Ekman pumping. c) Accumulated theoretical lift of a water parcel starting at the bottom of the Ekman layer due to Ekman pumping (assuming a stationary water column). Start depth was chosen as 49 m corresponding to the average depth of one of the CTD sensors on the 800 m mooring.

ume flux associated with AW eddies amount to around 0.1 Sv for the area from 0 to 45° E; based on the findings in *Crews et al.* [2018] a rough estimate for our study region is thus 0.03 Sv. Therefore, even though the overall loss of AW from the boundary current for the area studied by *Crews et al.* [2018] might be significant, the model-based estimates indicate that the local loss in our study region is on the order of 1% of the volume flux of AW in the boundary current [3.0 ± 0.2 Sv; *Beszczynska-Möller et al.*, 2012].

Eddies can be identified in a mooring time series as concurrent anomalies in temperature or salinity and across-slope velocity. In the records from the 800 m mooring, only one clear example of an anticyclonic (warm-core) eddy was detected as a semi-concurrent drop in temperature and increased up-slope velocity followed by an increase in temperature and down-slope velocity. Examples of current meandering are, however, plentiful. In these cases, strong decreases in temperature are followed by a return to mean values without an ensuing positive temperature anomaly which would be indicative of warmer water being moved away from the AW core. The lack of eddy signatures in our data suggests that warm-core eddies detach further off-shelf than our moorings, i.e. closer to the maximum gradient between the AW boundary current and the colder and fresher waters over the deeper slope and basin.

## 4 Discussion and Conclusions

The continental slope region north and northeast of Svalbard is crucial for modification of Atlantic Water at the beginning of its journey as a boundary current circulating throughout the Arctic Ocean. Fig. 11 presents a summary schematic of the relevant processes for the AW heat budget in sea ice-free autumn and winter and ice-covered spring and early summer conditions as presented in Section 3 and discussed in this section. From mooring records at 22 and 31° E, we estimate an annual mean heat loss of the upper ocean above the AW core towards the surface of 16.7 $\mathrm{Wm^{-2}}$ with shorter events having an order of magnitude larger vertical heat fluxes. This heat loss manifests itself as an average temperature difference between the two mooring locations of about 0.8° C at 50 m depth and 0.5° C for the maximum temperature in the AW core. *Cokelet et al.* [2008] found higher values from observations conducted in October-November 2001, whereas *Pérez-Hernández et al.* [2017] did not find a clear decrease in the average AW core temperature in September 2013. This illustrates the large temporal variability in heat loss but also corresponds well with the higher fluxes we find in late fall and winter.

From two different approaches to calculate heat loss during the passage from 22 to 31° E, we find enhancement of heat loss in the near-surface layer above 50 m. In two particular periods, estimates based on 50 m temperatures suggest heat loss of $> 50\,\mathrm{Wm^{-2}}$. In the first case, October-November, this can be related to an increase in negative air-sea heat flux, leading to a cooling of the surface layer as can be expected for autumn. As this seasonal change occurs on large temporal and spatial scales, the signal in the ocean is observable at both moorings. During the second period (February-March) however, the eastern mooring is at first covered by sea ice whereas the upstream mooring is in open water. There, SST is markedly higher. The following ice free period of elevated heat loss at the eastern mooring results in low surface layer temperatures and thus large temperature differences between the moorings. The subsequent high heat loss estimates, however, are at this time forced by local effects, overriding the advective signal.

Vertical fluxes derived from current shear and hydrography for autumn and early winter support the enhancement of heat loss towards the surface. Autumn observations of turbulent fluxes in this area are largely non-existent. Some distance upstream, *Sirevaag and Fer* [2009] found values of the same order of magnitude during spring, and episodes with significantly enhanced vertical heat flux were observed during the N-ICE2015 experiment in January-June 2015 [*Meyer et al.*, 2017; *Provost et al.*, 2017], when the drifting ice camp traveled over inflowing AW. These episodes were connected to major storm events

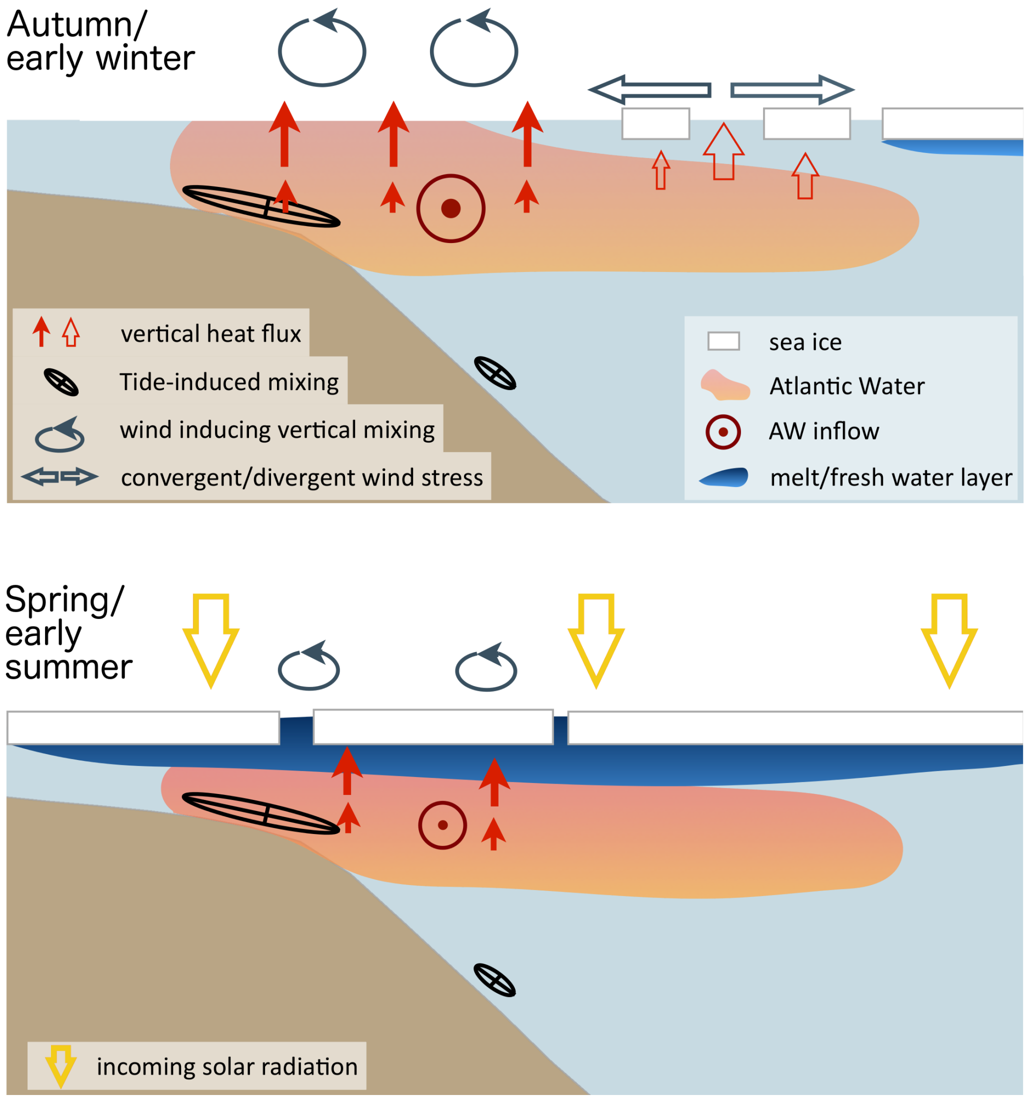


**Figure 11.** Illustration of the main processes influencing AW heat content during autumn to early winter (top) and spring to early summer (bottom) over the continental shelf and slope north of Svalbard. Vertical heat loss from the AW core upwards is mainly driven by wind-induced mixing (grey wind arrows, solid red arrows). Ekman pumping by divergent wind stress (grey open arrows) is a minor source of vertical heat flux (open red arrows). Tide-induced mixing (black tidal ellipses) is significant on the shelf, but much smaller in deeper parts. In spring/early summer, a melt water layer under the ice strongly impacts the stratification and hence mixing and vertical heat flux above the AW core. Extensive sea ice cover limits fluxes to the atmosphere and transfer of wind momentum. Solar radiation (yellow open arrows) becomes important toward late spring/early summer.

and led to significant basal sea ice melt. The agreement between the upper-ocean vertical heat flux estimates and air-sea fluxes during ice-free periods, and the differences connected to the presence of sea ice and changes in wind conditions demonstrate the influence of local environmental conditions.

Tidal analysis of the mooring current measurements shows significant differences between the shelf break/upper slope and the core of the AW current/deeper slope. While we cannot quantify dissipation and vertical heat fluxes based on our data (except for the upper part of the 800 m mooring thanks to mooring blow down in autumn), our findings support earlier measurements of tidally-driven upper-slope enhancement of mixing and vertical heat flux in this area [*Rippeth et al.*, 2015]. Such tidal mixing has also been inferred farther downstream over the Laptev Sea slope, where tides are weaker but the shelf break shallower [*Dmitrenko et al.*, 2011]. Enhanced vertical mixing near the shelf break would, in addition to efficiently bringing heat upwards, increase the potential energy over the upper slope relative to the deeper slope. This would tend to set up an off-slope pressure gradient in the upper part of the water column that, when taking rotational effects into account, would serve to enhance the along-slope flow high in the water column relative to the flow over the bottom. The comparatively strong tides and large dissipation in our study area could thus be seen as supporting the observed conversion from predominantly barotropic to more baroclinic flow between Fram Strait and the area north of Svalbard [*Pnyushkov et al.*, 2013]. The contrast we find in vertical distribution of tidal velocities between ice-free and ice-covered – stratified and less stratified – periods (Fig. 8) indicates that the role of tides for vertical mixing may be reduced with a shift to shorter ice covered periods. On the other hand, less ice and melt water may allow for increased wind-driven vertical heat flux, both in the mixing layer and through internal waves. The downstream effects of longer open water periods north of Svalbard appear to be discernible already [*Polyakov et al.*, 2017], apparently overriding the possible reduction in mixing resulting from lower vertical tidal current shear.

Sea ice acts as a barrier for heat exchange between the atmosphere and the ocean. However, a partial ice cover can actually enhance transfer of wind stress into the ocean as observed by *Schulze and Pickart* [2012]. *Martin et al.* [2014] confirm this in a model study, and suggest that ice concentrations between 80 and 90% are optimal for momentum transfer whereas above 90%, transfer is inhibited. Unfortunately, we do not have dissipation and resulting heat flux estimates for the period in February, when ice concentrations are in that range, and the 50 m temperature differences between 22 and 31° E suggest high heat flux, but we could speculate that the mobile ice cover actually helps to reduce the developing stratification in the surface layer. In periods when the ice cover is extensive over the AW boundary current, we see that the increased stratification due to melt water input in the surface layer suppresses vertical heat flux. In years with larger transport of sea ice to the slope region, i.e. a longer ice covered period, we therefore expect the heat loss from the AW boundary current to be lower compared to years with less sea ice. More of the incoming AW heat can thus be retained for the onward journey. In years with less sea ice, as in several of the recent years, one would expect deeper wind-driven mixing and less pronounced stratification between surface and the AW core, in line with findings from the Laptev Sea slope [*Polyakov et al.*, 2017].

*Schulze and Pickart* [2012] connect sea ice cover and wind stress to upwelling characteristics in the Alaskan Beaufort Sea. In a numerical study, *Carmack and Chapman* [2003] showed how the retreat of the sea ice edge beyond the shelf break enables increased shelf-break upwelling under favourable wind conditions in that region. *Våge et al.* [2016] suggested that the CTD surveys during the deployment cruise for our mooring array show indications of upwelling. However, analysing the mooring record, we are not able to confirm the occurrence of shelf break upwelling events.

Independent of geographical constraints, wind-induced Ekman pumping has the potential to influence vertical heat fluxes. *Yang* [2006] showed in an Arctic-wide study how divergent and convergent Ekman transport and associated pumping varied significantly both seasonally and spatially, with highest vertical velocities in autumn and winter in the Beaufort Sea and in Fram Strait. The eastern Fram Strait is dominated by positive pumping, but this is reduced farther to the east at our mooring location. In general though, the southern Nansen Basin and the region north of Svalbard are at least seasonally likely to experience vertical heat flux due to Ekman transport. We find relatively modest but non-negligible offshore net upward pumping. Following *Yang* [2006] to calculate upward heat flux associated with this Ekman pumping, we estimate an average heat loss of 3.5 $\mathrm{Wm^{-2}}$ from 30 m depth. While offshore Ekman pumping does not currently seem to be a major driver of heat exchange north of Svalbard, *Ma et al.* [2017] report an increase of vertical velocities driven by Ekman transport with eastern Fram Strait being one of the regions with large increases in upward pumping. *Lind and Ingvaldsen* [2012] found Ekman pumping to be a major driver for AW entering the Barents Sea from the north, and a strengthening of this pumping might contribute to further warming of the Barents Sea.

The very large local autumn and winter heat loss calculated from our in situ measurements along the upper slope north of Svalbard are consistent with the findings of *Ivanov et al.* [2012] and *Onarheim et al.* [2014] who argued that winter ice loss north of Svalbard is driven from below by AW inflow. In fact, Figure 3 in *Onarheim et al.* [2014] shows that the ice loss is largest in the months October to February, the period in which both AW heat content and heat loss in our mooring record is largest.

We presented year-long records from moorings deployed north of Svalbard in the inflow of Atlantic Water into the Arctic. Our observations document variability in the core of the AW inflow and its heat content. Advection of signals from further upstream accounts for over 80% of the variability in our time series. However, local processes have significant impact on the higher frequency variability. This includes air-sea heat exchange, wind- and tidally driven mixing (Fig. 11). The high flux values inferred from internal wave parameterisation and air-sea reanalysis indicate that the bulk of the heat loss is vertical and not lateral. As seen in autumn 2012, episodes of increased advection and strong wind significantly increase the annual mean heat loss. Sea ice plays a major role by impacting these processes to varying degrees and depending on ice concentrations. A longer time series spanning several years is necessarily to better distinguish seasonal signals, and assess changes in the AW inflow and their impact downstream in the Arctic. Our results also demonstrate the need for continuous year-round observations, as significant short-duration episodes of elevated vertical heat fluxes, e.g. during storms and in winter, are usually not captured by shipboard surveys, which therefore will not allow for heat content and transport estimates that are representative for longer time periods.

**Acknowledgments**

We thank the captain and crews of RV Lance, Kristen Fossan, Ronald Pedersen for the technical support with the mooring deployments and cruises. We are grateful to Vladimir Pavlov for help with data processing and discussions during early stages of the manuscript. The A-TWAIN project is financially supported by the Fram Centre flagship "Sea ice in the Arctic Ocean, technology and agreements". The analysis was partially funded by the Research Council of Norway through the project The Nansen Legacy (RCN #276730). The US component of A-TWAIN was funded by the National Science Foundation under grant ARC-1264098 as well as a grant from the Steven Grossman Family Foundation. The IOPAN contribution to A-TWAIN observations and data analyses was supported by the Polish-Norwegian Research Programme under the project PAVE (Atlantic Water Pathways to the Arctic: Variability and Effects on Climate and Ecosystems, contract no. POL-NOR/202006/10/2013). The mooring data are available from the Norwegian Polar Data Centre [*Sundfjord et al.*, 2017].

## References


Aagaard, K. (1989), A synthesis of the Arctic Ocean circulation, *Rapp. P.-v. Réun. Cons. int. Explor. Mer*, *188*, 11–22.

Aagaard, K., A. Foldvik, and S. R. Hillman (1987), The West Spitsbergen Current: Disposition and water mass transformation, *Journal of Geophysical Research: Oceans*, *92(C4)*, 3778–3784.

Aksenov, Y., V. V. Ivanov, A. J. G. Nurser, S. Bacon, I. V. Polyakov, A. C. Coward, A. C. Naveira Garabato, and A. Beszczynska Moeller (2011), The Arctic Circumpolar Boundary Current, *Journal of Geophysical Research*, *116, C09017*, doi:10.1029/2010JC006637.

Beszczynska-Möller, A., E. Fahrbach, U. Schauer, and E. Hansen (2012), Variability in Atlantic water temperature and transport at the entrance to the Arctic Ocean, 1997-2010, *ICES Journal of Marine Science*, *69(5)*, 852–863, doi:10.1093/icesjms/fss056.

Carmack, E., and D. C. Chapman (2003), Wind-driven shelf/basin exchange on an Arctic shelf: The joint roles of ice cover extent and shelf-break bathymetry, *Geophysical Research Letters*, *30(14),1778*, doi:10.1029/2003GL017526.

Cokelet, E. D., N. Tervalon, and J. G. Bellingham (2008), Hydrography of the West Spitsbergen Current, Svalbard Branch: Autumn 2001, *Journal of Geophysical Research*, *113, C01006*, doi:10.1029/2007JC004150.

Crews, L., A. Sundfjord, J. Albretsen, and T. Hattermann (2018), Mesoscale eddy activity and transport in the Atlantic Water inflow region North of Svalbard, *Journal of Geophysical Research: Oceans*, *123(1)*, 201–215, doi:10.1002/2017JC013198.

Dee, D. P., S. M. Uppala, A. J. Simmons, P. Berrisford, P. Poli, S. Kobayashi, U. Andrae, M. A. Balmaseda, G. Balsamo, P. Bauer, P. Bechtold, A. C. M. Beljaars, L. van de Berg, J. Bidlot, N. Bormann, C. Delsol, R. Dragani, M. Fuentes, A. J. Geer, L. Haimberger, S. B. Healy, H. Hersbach, E. V. Hólm, L. Isaksen, P. Kållberg, M. Köhler, M. Metricardi, A. P. McNally, B. M. Monge-Sanz, J. J. Morcrett, B.-K. Park, C. Peubey, P. de Rosnay, C. Tavolato, J.-N. Thépaut, and F. Vitart (2011), The ERA-Interim reanalysis: configuration and performance of the data assimilation system, *Quarterly Journal of the Royal Meteorological Society*, *137*, 553–597, doi:10.1002/qj.828.

Dmitrenko, I. A., I. V. Polyakov, S. A. Kirillov, L. A. Timokhov, H. L. Simmons, V. V. Ivanov, and D. Walsh (2006), Seasonal variability of Atlantic water on the continental slope of the Laptev Sea during 2002-2004, *Earth and Planetary Science Letters*, *224(3-4)*, 735–743, doi:10.1016/j.epsl.2006.01.067.

Dmitrenko, I. A., V. V. Ivanov, S. A. Kirillov, E. L. Vinogradova, S. Torres-Valdes, and D. Bauch (2011), Properties of the Atlantic derived halocline waters over the Laptev Sea continental margin: Evidence from 2002 to 2009, *Journal of Geophysical Research*, *116, C10024*, doi:10.1029/2011JC007269.

Gascard, J. C., C. Richez, and C. Rouault (1995), New insights on large-scale oceanography in Fram Strait: the West Spitsbergen Current, in *Arctic oceanography: marginal ice zones and continental shelves*, edited by W. O. Smith and J. M. Grebmeier, pp. 131–182, American Geophysical Union, Washington D. C.

Gonella, J. (1972), A rotary-component method for analysing meteorological and oceanographic vector time series, *Deep-Sea Research*, *19*, 833–846.

Guest, P. S., J. W. Glendening, and K. L. Davidson (1995), An observational numerical study of wind stress variations within marginal ice zones, *Journal of Geophysical Research*, *100*, 10,887–10,904.

Hattermann, T., P. E. Isachsen, W.-J. von Appen, J. Albretsen, and A. Sundfjord (2016), Eddy-driven recirculation of Atlantic Water in Fram Strait, *Geophysical Research Letters*, *43*, doi:10.1002/2016GL068323.

Henyey, F. S., J. Wright, and S. M. Flatté (1986), Energy and action flow through the internal wave field: An eikonal approach, *Journal of Geophysical Research*, *91(C7)*, 8487–8495, doi:10.1029/JC091iC07p08487.

Hudson, S. R., M. A. G. A. Sundfjord, A. Randelhoff, A. H. H. Renner, and D. V. Divine (2013), Energy budget of first-year Aarctic sea ice in advanced stages of melt, *Geophysical Research Letters*, *40*, 2679–2683, doi:10.1002/grl.50517.

Ivanov, V., V. Alexeev, N. Y. Koldunov, I. Repina, A. B. Sandø, L. H. Smedsrud, and A. Smirnov (2016), Arctic Ocean heat impact on regional ice decay: a suggested positive feedback, *Journal of Physical Oceanography*, *46*, 1437–1456, doi:10.1175/JPO-D-15-0144.1.

Ivanov, V. V., I. V. Polyakov, I. A. Dmitrenko, H. E., I. A. Repina, S. A. Kirillov, C. Mauritzen, H. Simmons, and L. A. Timokhov (2009), Seasonal variability in Atlantic Water off Spitsbergen, *Deep-Sea Research I*, *56*, 1–14, doi:10.1016/j.dsr.2008.07.013.

Ivanov, V. V., V. A. Alexeev, I. Repina, N. V. Koldunov, and A. Smirnov (2012), Tracing Atlantic Water signature in the Arctic sea ice cover east of Svalbard, *Advances in Meteorology*, *2012*, doi:10.1155(2012/201818.

Jakobsson, M. e. a. (2012), The Internaltional Bathymetric Chart of the Arctic Ocean (IBCAO) Version 3.0, *Geophysical Research Letters*, *39, L12609*, doi:10.1029/2012GL052219.

Janout, M., J. Hölemann, B. Juhls, T. Krumpen, R. B., D. Bauch, C. Wegner, H. Kassens, and L. Timokhov (2016), Episodic warming of near-bottom waters under the Arctic sea ice on the central Laptex Sea shelf, *Geophysical Research Letters*, *43*, 264–272, doi:10.1002/2015GL066565.

Janout, M. A., and Y.-D. Lenn (2014), Semidiurnal tides on the Laptev Sea shelf with implications for shear and vertical mixing, *Journal of Physical Oceanography*, *44*, 202–219, doi:10.1175/JPO-D-12-0240.1.

Koenig, Z., C. Provost, N. Villacieros-Robineau, N. Sennéchael, and A. Meyer (2016), Winter ocean-ice interactions under thin sea ice observed by IAOOS platforms during N-ICE2015: Salty surface mixed layer and active basal melt, *Journal of Geophysical Research*, *121(10)*, 7898–7916, doi:10.1002/2016JC012195.

Koenig, Z., C. Provost, N. Sennéchael, G. Garric, and J.-C. Gascard (2017), The Yermak Pass Branch: A major pathway for the Atlantic Water north of Svalbard, *Journal of Geophysical Research Oceans*, *122*, 9332–9349, doi:10.1002/2017JC013271.

Lenn, Y. D., P. J. Wiles, S. Torres-Valdes, E. P. Abrahamsen, T. P. Rippeth, J. H. Simpson, S. Bacon, S. W. Laxon, I. Polyakov, V. Ivanov, and S. Kirillov (2009), Vertical mixing at intermediate depths in the Arctic boundary current, *Geophysical Research Letters*, *36, L05601*, doi:10.1029/2008GL036792.

Lenn, Y.-D., T. P. Rippeth, C. P. Old, S. Bacon, I. Polyakov, V. Ivanov, and J. Hölemann (2011), Intermittent intense turbulent mixing under ice in the Laptev Sea continental shelf, *Journal of Physical Oceanography*, *41*, 531–547, doi:10.1175/2010JPO4425.1.

Lin, P., R. S. Pickart, G. W. K. Moore, M. A. Spall, and J. Hu (2018), Characteristics and dynamics of wind-driven upwelling in the Alaskan Beaufort Sea based on six years of mooring data, *Deep Sea Research II*, doi:10.1016/j.dsr2.2018.01.002.

Lind, S., and R. B. Ingvaldsen (2012), Variability and impacts of Atlantic Water entering the Barents Sea from the north, *Deep Sea Research I*, *62*, 70–88, doi:10.1016/j.dsr.2011.12.007.

Luneva, M. V., Y. Aksenov, J. D. Harle, and J. T. Holt (2015), The effects of tides on the water mass mixing and sea ice in the Arctic Ocean, *Journal of Geophysical Research*, *120*, doi:10.1002/2014JC010310.

Ma, B., M. Steele, and C. M. Lee (2017), Ekman circulation in the Arctic Ocean: Beyond the Beaufort Gyre, *Journal of Geophysical Research: Oceans*, *122*, 3358–3374, doi:10.1002/2016JC012624.

Martin, T., M. Steele, and J. Zhang (2014), Seasonality and long-term trend of Arctic Ocean surface stress in a model, *Journal of Geophysical Research: Oceans*, *119*, 1723–1738, doi:10.1002/2013JC009425.

Meyer, A., I. Fer, A. Sundfjord, and A. K. Peterson (2017), Mixing rates and vertical heat fluxes north of Svalbard from Arctic winter to spring, *Journal of Geophysical Research*, *122*, doi:10.1002/2016JC012441.

Nøst, O. A., and P. E. Isachsen (2003), The large-scale time-mean ocean circulation in the Nordic Seas and Arctic Ocean estimated from simplified dynamics, *Journal of Marine Research*, *61*, 175–201.

Onarheim, I., L. Smedsrud, R. Ingvaldsen, and F. Nilsen (2014), Loss of sea ice during winter north of svalbard, *Tellus A*, *66*, doi:10.3402/tellusa.v66.23933.

Osborn, T. R. (1980), Estimates of the local rate of vertical diffusion from dissipation measurements, *Journal of Physical Oceanography*, *10(1)*, 83–89.

Padman, L., and S. Erofeeva (2003), A barotropic inverse tidal model for the Arctic Ocean, *Geophysical Research Letters*, *31, L02303*, doi:10.1029/2003GL019003.

Pawlowicz, R., B. Beardsley, and S. Lentz (2002), Harmonic analysis including error estimates in MATLAB unsing T_ TIDE, *Computers and Geosciences*, *28*, 929–937.

Pérez-Hernández, M. D., R. S. Pickart, V. Pavlov, K. Våge, R. Ingvaldsen, A. Sundfjord, A. H. H. Renner, D. J. Torres, and S. Y. Erofeeva (2017), The Atlantic Water boundary current north of Svalbard in late summer, *Journal of Geophysical Research*, *122*, 2269–2290, doi:10.1002/2016JC012486.

Peterson, A. K., I. Fer, M. G. McPhee, and A. Randelhoff (2017), Turbulent heat and momentum fluxes in the upper ocean under Arctic sea ice, *Journal of Geophysical Research*, doi:10.1002/2016JC012283.

Pickart, R. S., G. W. K. Moore, D. J. Torres, P. S. Fratantoni, R. A. Goldsmith, and J. Yang (2009), Upwelling on the continental slope of the Alaskan Beaufort Sea: storms, ice, and oceanographic response, *Journal of Geophysical Research*, *114, C00A13*, doi:10.1029/2008JC005009.

Pickart, R. S., M. A. Spall, and J. T. Mathis (2013), Dynamics of upwelling in the Alaskan Beaufort Sea and associated shelf-basin fluxes, *Deep-Sea Research I*, *76*, 35–51.

Pnyushkov, A. V., and I. V. Polyakov (2012), Observations of tidally induced currents over the continental slope of the Laptev Sea, Arctic Ocean, *Journal of Physical Oceanography*, *42*, 78–94, doi:10.1175/JPO-D-11.064.1.

Pnyushkov, A. V., I. V. Polyakov, V. V. Ivanov, and T. Kikuchi (2013), Structure of the Fram Strait branch of the boundary current in the Eurasian Basin of the Arctic Ocean, *Polar Science*, *7*, 53–71, doi:10.1016/j.polar.2013.02.001.

Pnyushkov, A. V., I. V. Polyakov, V. V. Ivanov, Y. Aksenov, A. C. Coward, M. Janout, and B. Rabe (2015), Structure and variability of the boundary current in the Eurasian Basin of the Arctic Ocean, *Deep-Sea Research I*, *101*, 80–97.

Polyakov, I. V., A. Beszczynska, E. C. Carmack, I. A. Dmitrenko, E. Fahrbach, I. E. Frolov, R. Gerdes, E. Hansen, J. Holfort, V. V. Ivanov, M. A. Johnson, M. Karcher, F. Kauker, J. Morison, K. A. Orvik, U. Schauer, H. L. Simmons, O. Skagseth, V. T. Sokolov, M. Steele, L. A. Timokhov, D. Walsh, and J. E. Walsh (2005), One more step toward a warmer Arctic, *Geophysical Research Letters*, *32, L17605*, doi:10.1029/2005GL023740.

Polyakov, I. V., L. A. Timokhov, V. A. Alexeev, S. Bacon, I. A. Dmitrenko, L. Fortier, I. E. Frolov, J.-C. Gascard, E. Hansen, V. V. Ivanov, S. Laxon, C. Mauritzen, D. Perovich, K. Shimada, H. L. Simmons, V. T. Sokolov, M. Steele, and J. Toole (2010), Arctic Ocean warming contributes to reduced polar ice cap, *Journal of Physical Oceanography*, *40*, 2743–2756, doi:10.1175/2010JPO4339.1.

Polyakov, I. V., A. V. Pnyushkov, M. B. Alkire, I. M. Ashik, T. M. Baumann, E. C. Carmack, I. Goszczko, J. Guthrie, V. V. Ivanov, T. Kanzow, R. Krishfield, R. Kwok, A. Sundfjord, J. Morison, R. Rember, and A. Yulin (2017), Greater role for Atlantic inflows on sea-ice loss in the Eurasian Basin of the Arctic Ocean, *Science*, doi:10.1126/science.aai8204.

Provost, C., N. Sennéchael, J. Miguet, P. Itkin, A. Rösel, Z. Koenig, N. Villacieros-Robineau, and M. A. Granskog (2017), Observations of flooding and snow-ice formation in a thinner Arctic sea ice regime during the N-ICE2015 campaign: influence of basal ice melt and storms, *Journal of Geophysical Research*, doi:10.1002/2016JC012011.

Randelhoff, A., and A. Sundfjord (2018), Short commentary on marine productivity at Arctic shelf breaks: upwelling, advection and vertical mixing, *Ocean Science*, *14*, 293–300, doi:10.5194/os-14-293-2018.

Randelhoff, A., A. Sundfjord, and M. Reigstad (2015), Seasonal variability and fluxes of nitrate in the surface waters over the arctic shelf slope, *Geophys. Res. Lett.*, *42*(9), 3442–3449, doi:10.1002/2015GL063655.

Renner, A. H. H., S. Hendricks, S. Gerland, J. Beckers, C. Haas, and T. Krumpen (2013), Large-scale ice thickness distribution of first-year sea ice in spring and summer north of Svalbard, *Annals of Glaciology*, *54(62)*, 13–18, doi:10.3189/2013AoG62A146.

Reynolds, R. W. (2009), What's New in Version 2. OISST Webpage, `http://www.ncdc.noaa.gov/sites/default/files/attachments/Reynolds2009_oisst_daily_v02r00_version2-features.pdf`.

Reynolds, R. W., T. M. Smith, C. Liu, D. B. Chelton, K. S. Casey, and M. G. Schlax (2007), Daily high-resolution-blended analyses for sea surface temperature, *Journal of Climate*, *20*, 5473–5496, doi:10.1175/JCLI-D-14-00293.1.

Rippeth, T. P., B. J. Lincoln, Y.-D. Lenn, J. A. M. Green, A. Sundfjord, and S. Bacon (2015), Tide-mediated warming of Arctic halocline by Atlantic heat fluxes over rough topography, *Nature Geoscience*, *8*, 191–194, doi:10.1038/ngeo2350.

Rudels, B., H. J. Friedrich, and D. Quadfasel (1999), The Arctic Circumpolar Boundary Current, *Deep-Sea Research II*, *46*, 1023–1062, doi:10.1016/S0967-0645(99)00015-6.

Rudels, B., M. Kohonen, U. Schauer, S. Pisarev, B. Rabe, and A. Wisotzki (2014), Circulation and transformation of Atlantic water in the Eurasian Basin and the contribution of the Fram Strait inflow branch to the Arctic Ocean heat budget, *Progress in Oceanography*, *132*, 128–152, doi:10.1016/j.pocean.2014.04.003.

Schauer, U., E. Fahrbach, S. Osterhus, and G. Rohardt (2004), Arctic warming through the Fram Strait: Oceanic heat transport from 3 years of measurements, *Journal of Geophysical Research*, *109, C06026*, doi:10.1029/2003JC001823.

Schulze, L. M., and R. S. Pickart (2012), Seasonal variation of upwelling in the Alaskan Beaufort Sea: Impact of sea ice cover, *Journal of Geophysical Research*, *117, C06022*, doi:10.1029/2012JC007985.

Sirevaag, A., and I. Fer (2009), Early spring oceanic heat fluxes and mixing observed from drift stations north of Svalbard, *Journal of Physical Oceanography*, *39*, 3049–3069, doi:10.1175/2009JPO4172.1.

Spreen, G., L. Kaleschke, and G. Heygster (2008), Sea ice remote sensing using AMSR-E 89 GHz channels, *Journal of Geophysical Research*, *113, C02S03*, doi:10.1029/2005JC003384.

Sundfjord, A., A. H. H. Renner, and A. Beszczynska-Möller (2017), A-TWAIN mooring hydrography and current data Sep 2012 - Sep 2013 [Data set]. Norwegian Polar Institute, `https://data.npolar.no/dataset/73d0ea3a-fd21-4eab-8eb9-1e033fefcd8e`, doi:10.21334/npolar.2017.73d0ea3a.

Tschudi, M., C. Fowler, J. Maslanik, J. S. Stewart, and W. Meier (2016, accessed 29 May 2018), *Polar Pathfinder Daily 25 km EASE-Grid Sea Ice Motion Vectors, Version 3. Subset October 2012 - March 2013.*, National Snow and Ice Data Center, Boulder, Colorado, USA. distributed in netCDF format by the Integrated Climate Data Center (ICDC), University of Hamburg, Hamburg, Germany, doi:10.5067/O57VAIT2AYYY.

Våge, K., R. S. Pickart, V. Pavlov, P. Lin, D. J. Torres, R. Ingvaldsen, A. Sundfjord, and A. Proshutinsky (2016), The Atlantic Water boundary current in the Nansen Basin: Transport and mechanisms of lateral exchange, *Journal of Geophysical Research*, *121*, 6946–6960, doi:10.1002/2016JC011715.

Vinje, T. (2001), Anomalies and trends of sea-ice extent and atmospheric circulation in the Nordic Seas during the period 1864-1998, *Journal of Climate*, *14*, 255–267.

Wijesekera, H., L. Padman, T. Dillon, M. Levine, C. Paulson, and R. Pinkel (1993), The application of internal-wave dissipation models to a region of strong mixing, *Journal of*

*Physical Oceanography*, *23(2)*, 269–286.
Yang, J. (2006), The seasonal variability of the Arctic Ocean Ekman transport and its role in the mixed layer heat and salt fluxes, *Journal of Climate*, *19*, 5366–5387.

**Figure 1.**

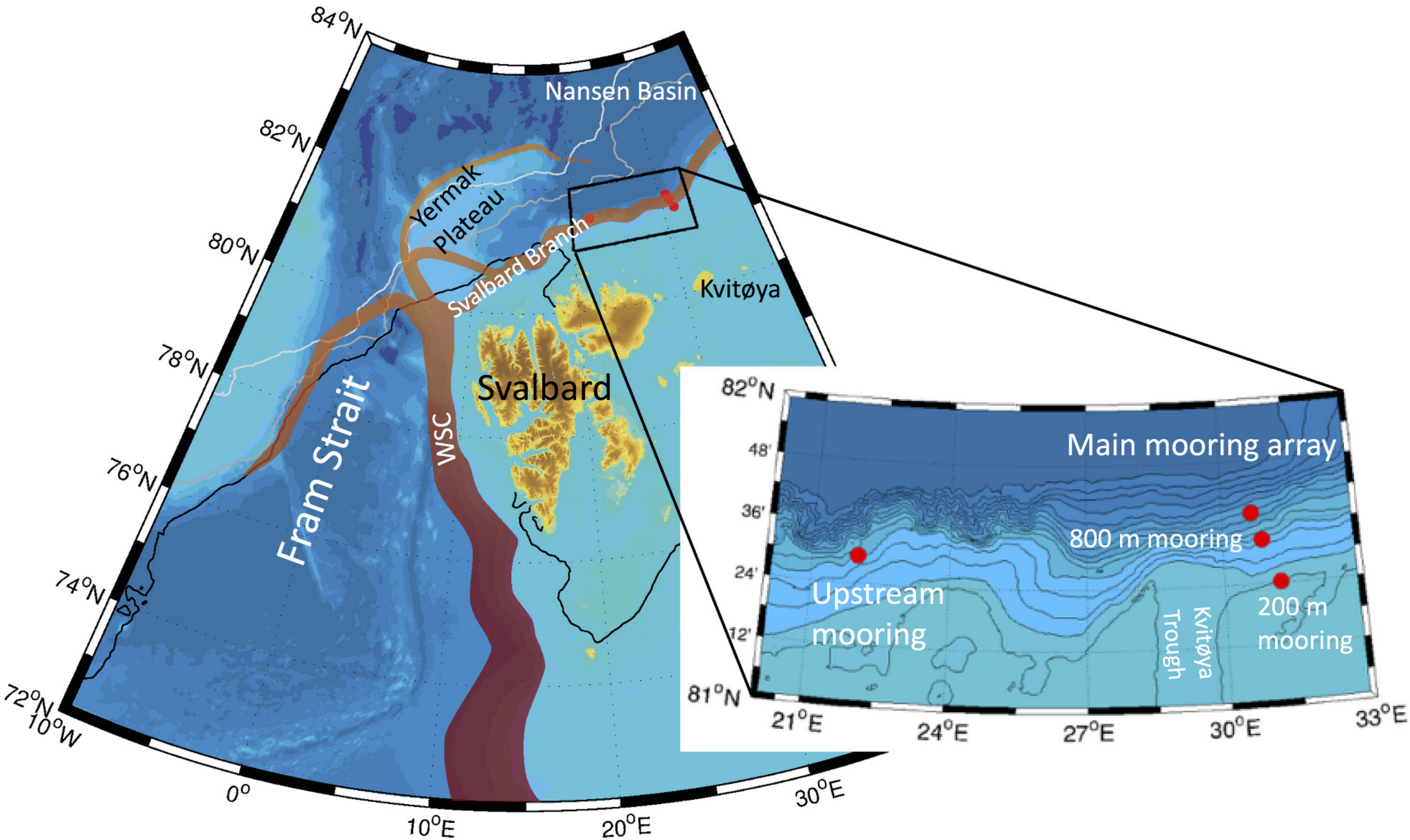
84°N
82°N
80°N
78°N
76°N
74°N
72°N
10°W
0°
10°E
20°E
30°E
Nansen Basin
Yermak Plateau
Svalbard Branch
Kvitøya
Svalbard
Fram Strait
WSC
82°N
48'
36'
24'
12'
81°N
21°E
24°E
27°E
30°E
33°E
Main mooring array
800 m mooring
Upstream mooring
200 m mooring
Kvitøya Trough

**Figure 2.**

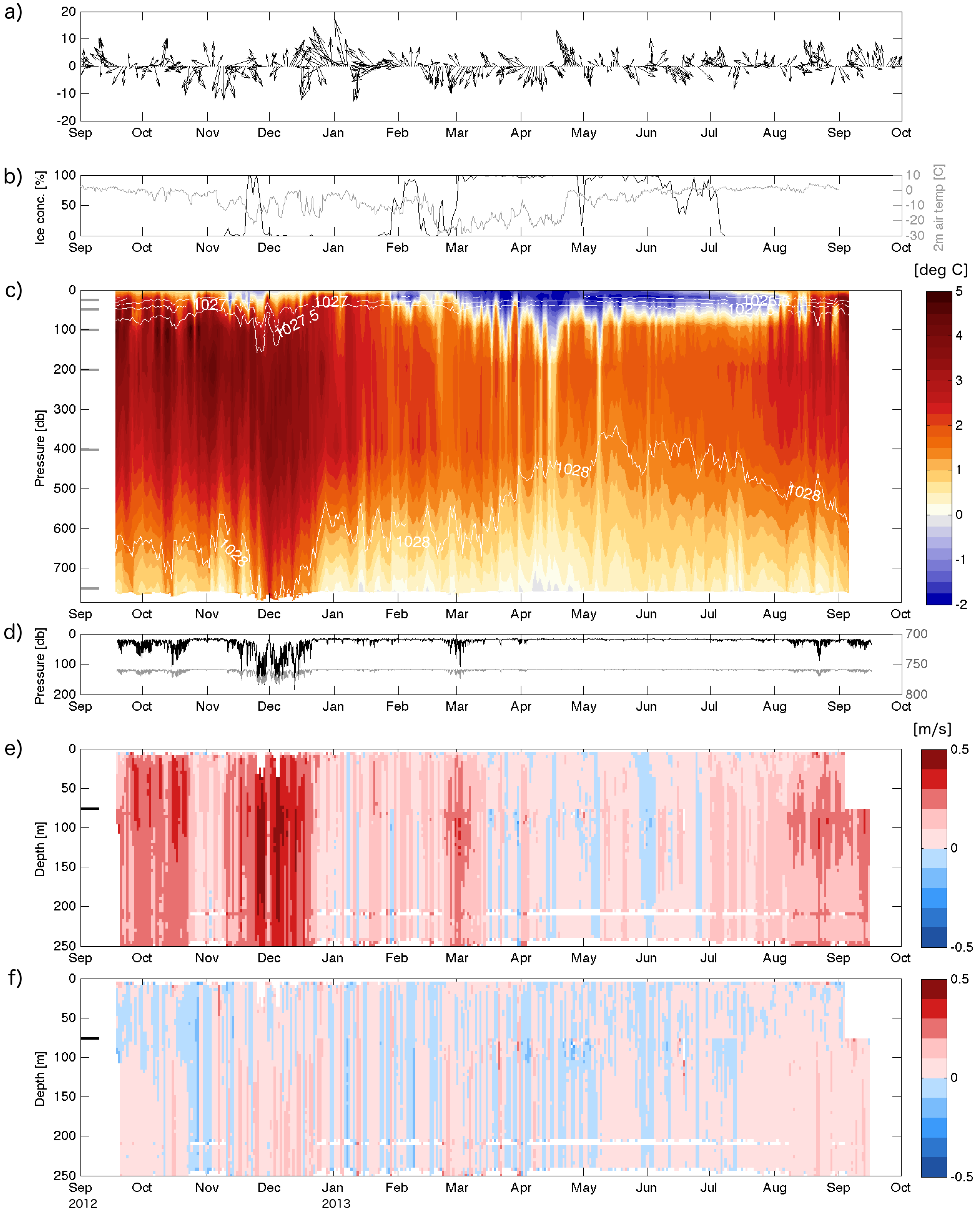

a)
20
10
0
-10
-20
Sep
Oct
Nov
Dec
Jan
Feb
Mar
Apr
May
Jun
Jul
Aug
Sep
Oct
b)
Ice conc. [%]
100
50
0
10
0
-10
-20
-30
2m air temp [C]
c)
Pressure [db]
0
100
200
300
400
500
600
700
1027
1027.5
1028
[deg C]
5
4
3
2
1
0
-1
-2
d)
Pressure [db]
0
100
200
700
750
800
e)
Depth [m]
0
50
100
150
200
250
[m/s]
0.5
0
-0.5
f)
Depth [m]
2012
2013

**Figure 3.**

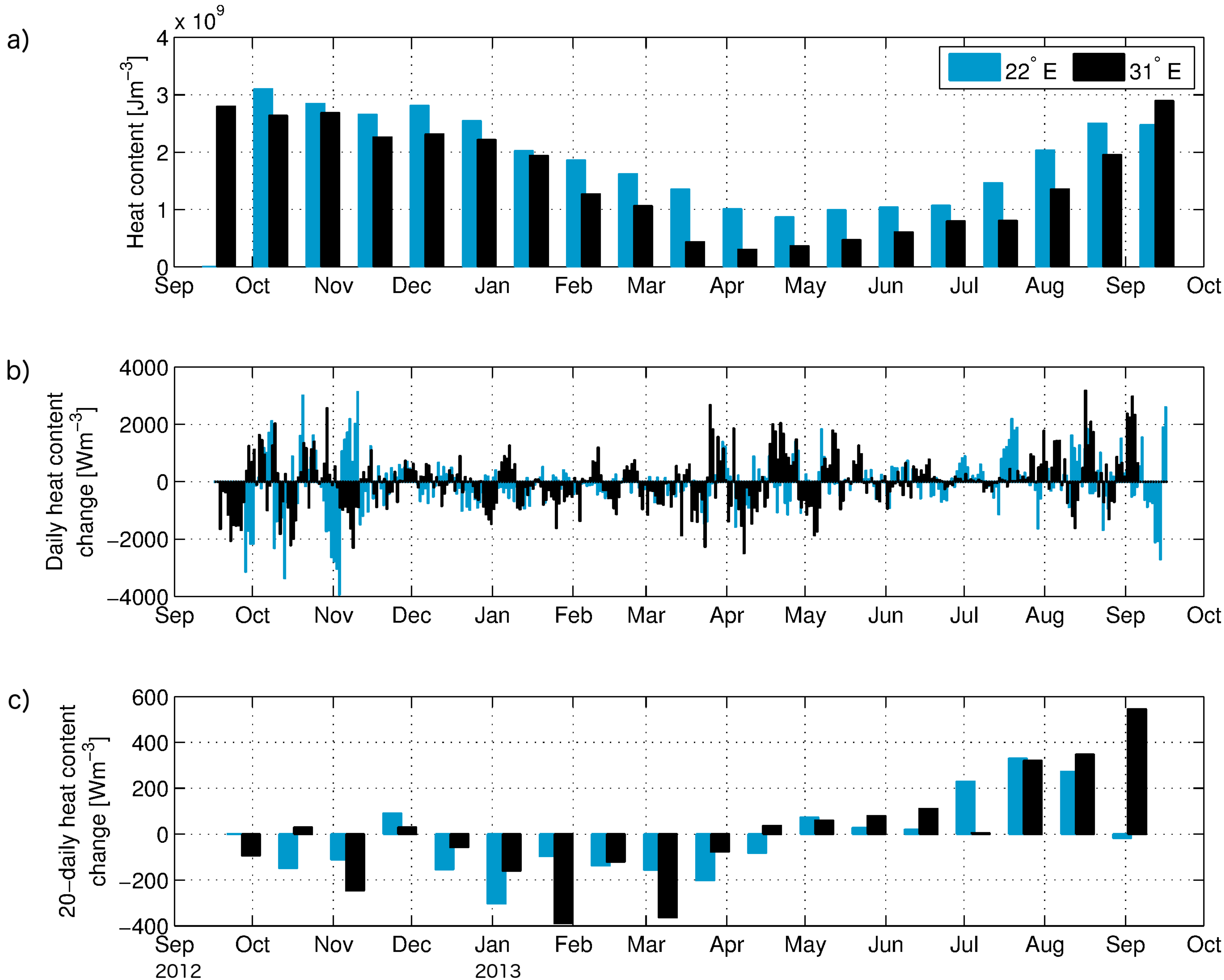

a)
b)
c)
x 10^9
Heat content [Jm^-3]
22° E
31° E
Daily heat content change [Wm^-3]
20-daily heat content change [Wm^-3]
Sep
Oct
Nov
Dec
Jan
Feb
Mar
Apr
May
Jun
Jul
Aug
Sep
Oct
2012
2013

**Figure 4.**

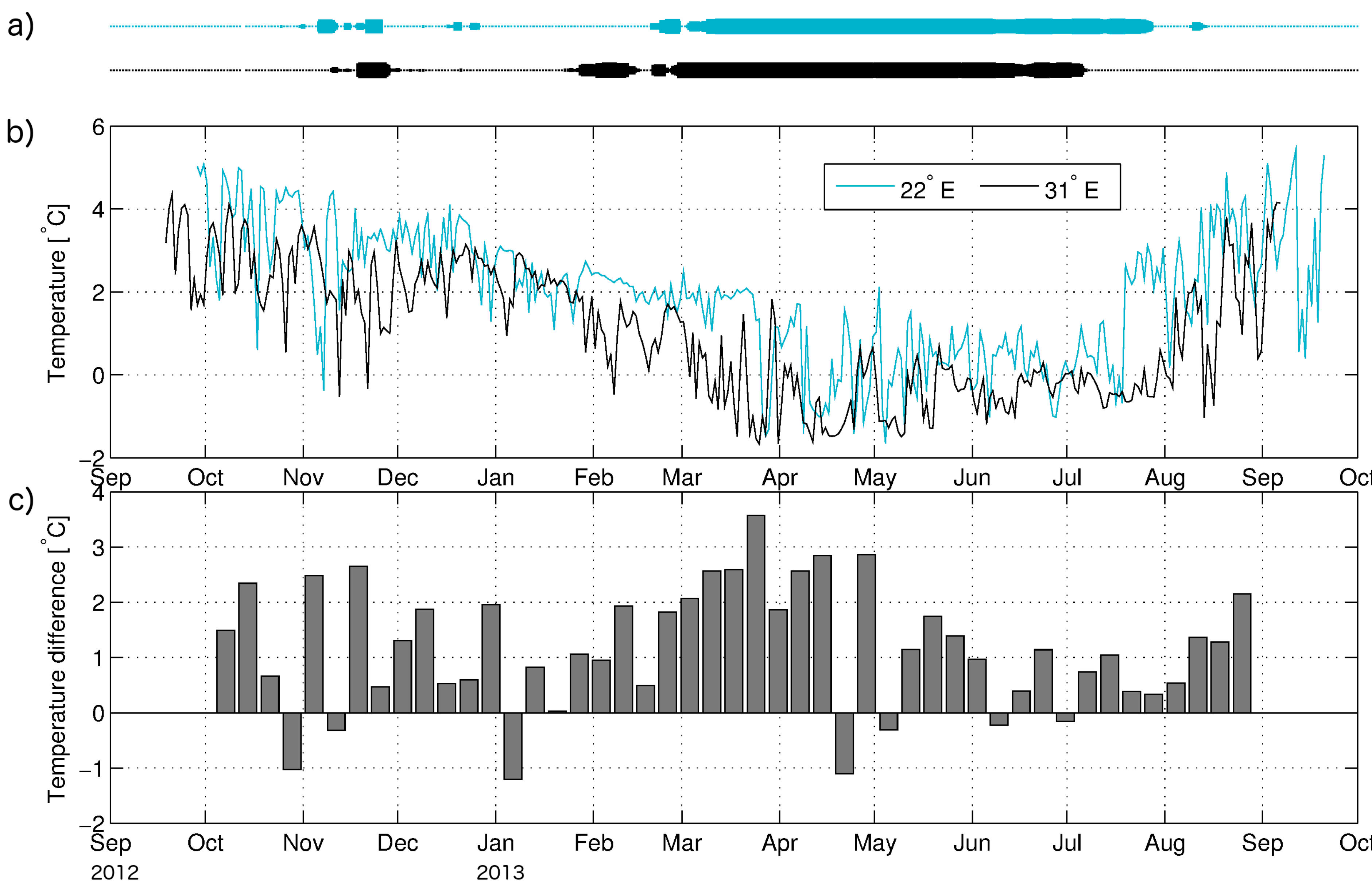
a)
b)
c)
22° E
31° E
Temperature [°C]
Temperature difference [°C]
6
4
2
0
−2
3
1
−1
Sep
Oct
Nov
Dec
Jan
Feb
Mar
Apr
May
Jun
Jul
Aug
Sep
Oct
2012
2013

**Figure 5.**

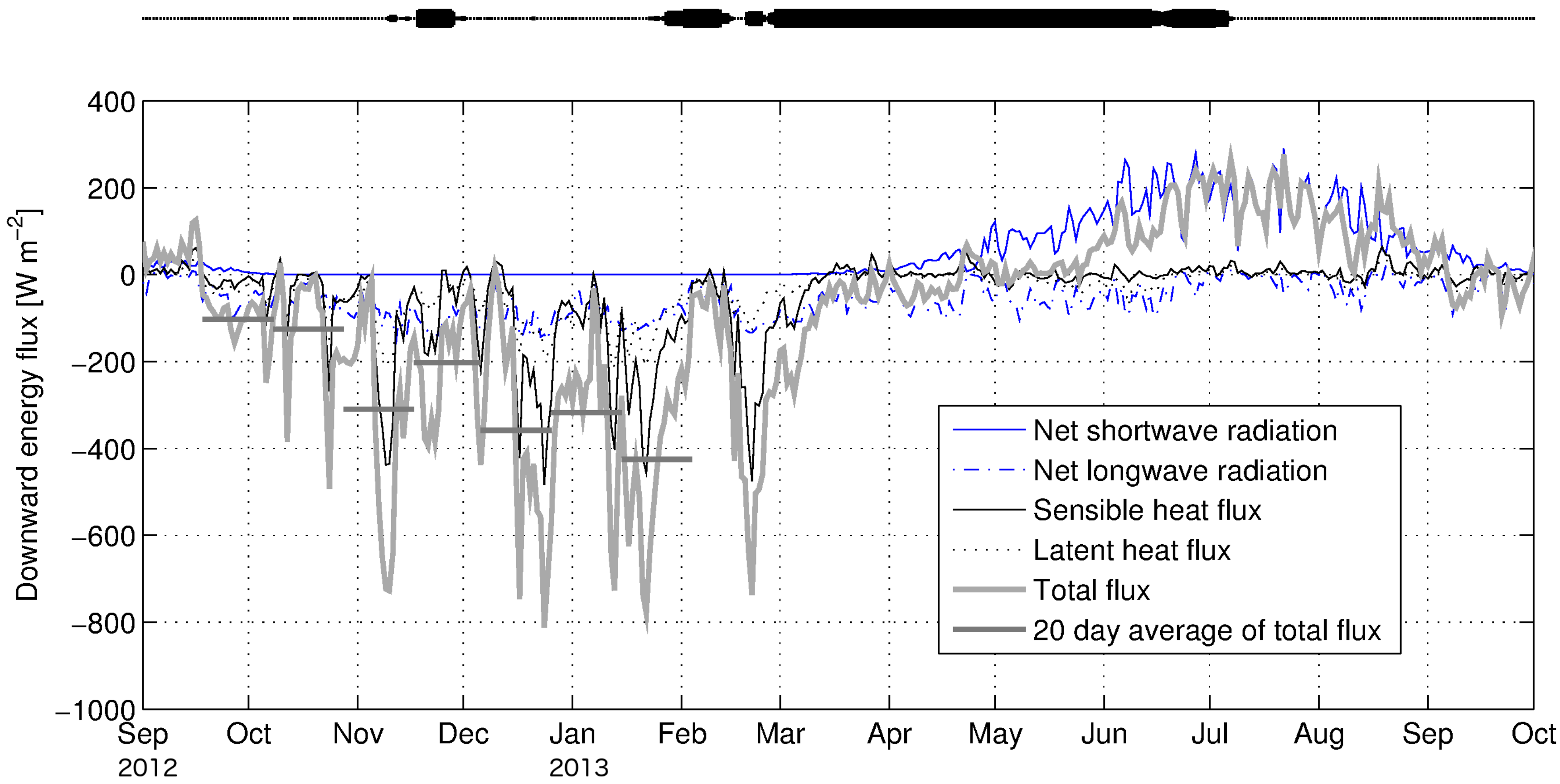

400
200
0
−200
−400
−600
−800
−1000
Downward energy flux [W m$^{-2}$]
Sep
2012
Oct
Nov
Dec
Jan
2013
Feb
Mar
Apr
May
Jun
Jul
Aug
Sep
Oct
Net shortwave radiation
Net longwave radiation
Sensible heat flux
Latent heat flux
Total flux
20 day average of total flux

**Figure 6.**

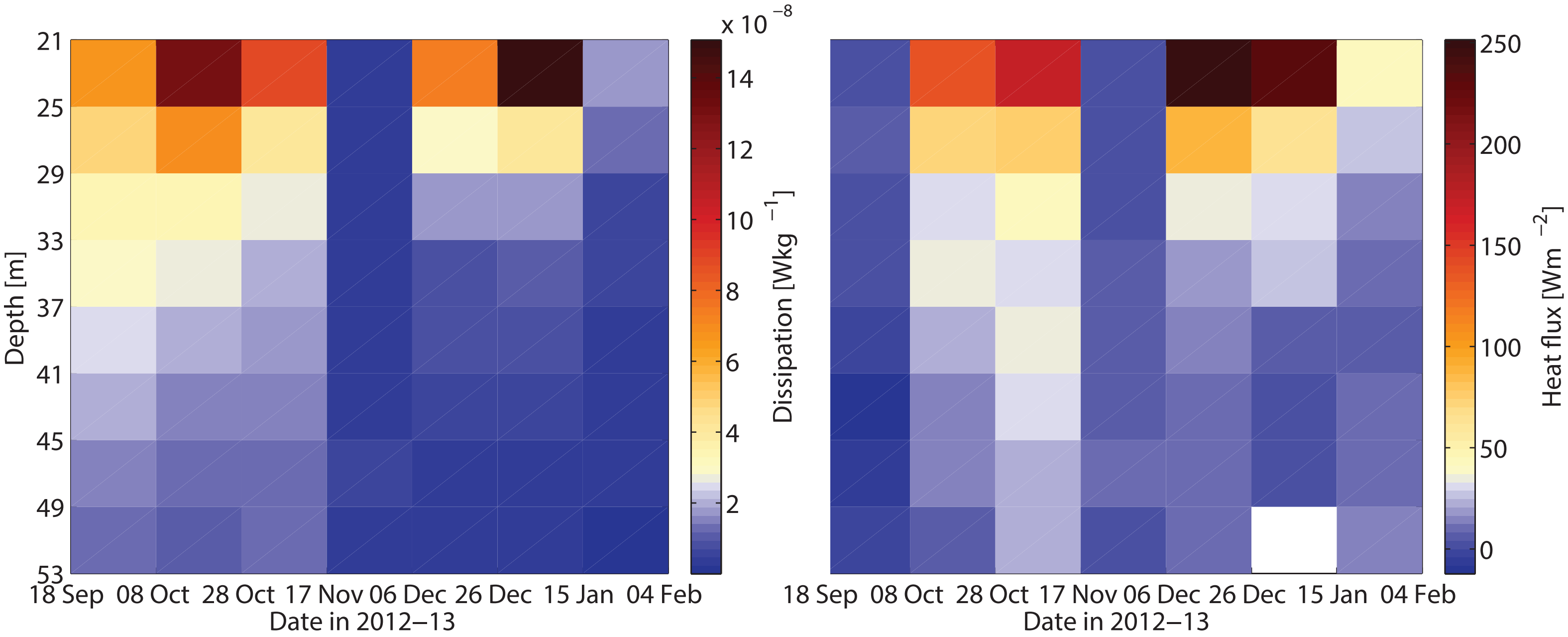

21
25
29
33
37
41
45
49
53
Depth [m]
18 Sep 08 Oct 28 Oct 17 Nov 06 Dec 26 Dec 15 Jan 04 Feb
Date in 2012–13
x 10 −8
14
12
10
8
6
4
2
Dissipation [Wkg −1]
18 Sep 08 Oct 28 Oct 17 Nov 06 Dec 26 Dec 15 Jan 04 Feb
Date in 2012–13
250
200
150
100
50
0
Heat flux [Wm −2]

**Figure 7.**

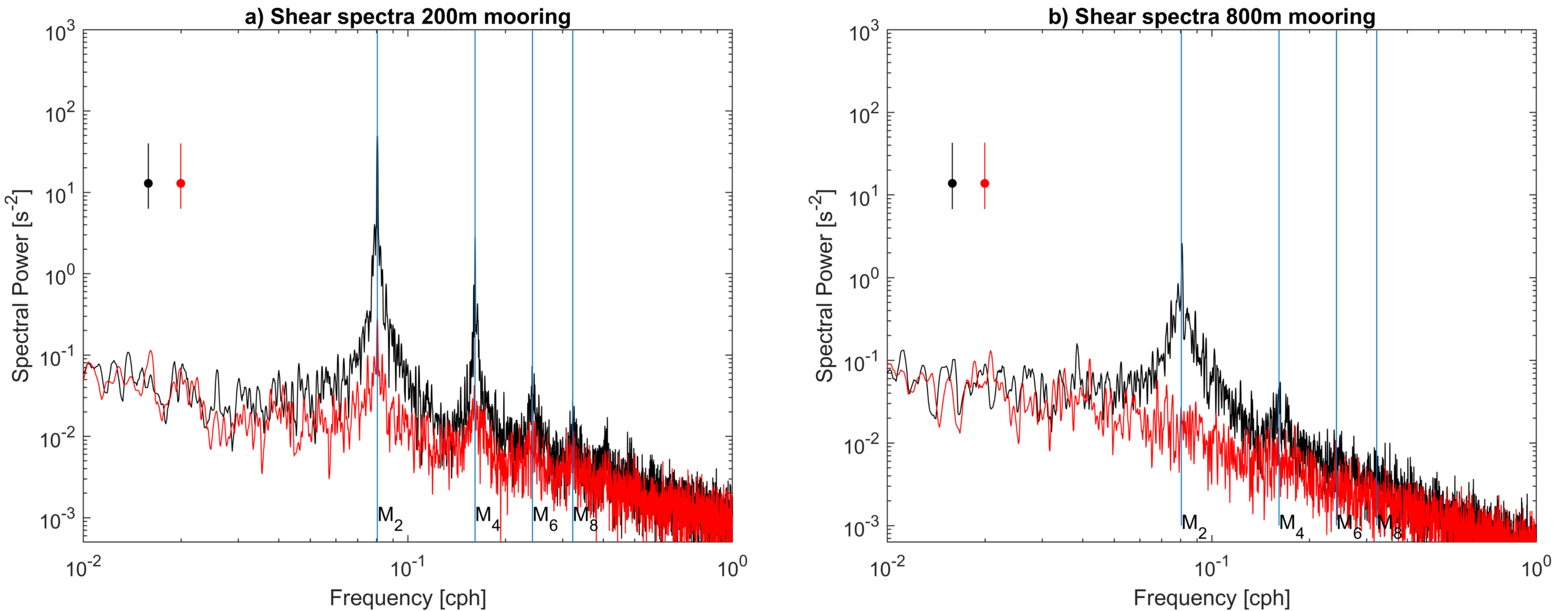

a) Shear spectra 200m mooring
b) Shear spectra 800m mooring
Spectral Power [s-2]
Frequency [cph]
M2
M4
M6
M8
10-2
10-1
100
10-3
101
102
103

**Figure 8.**

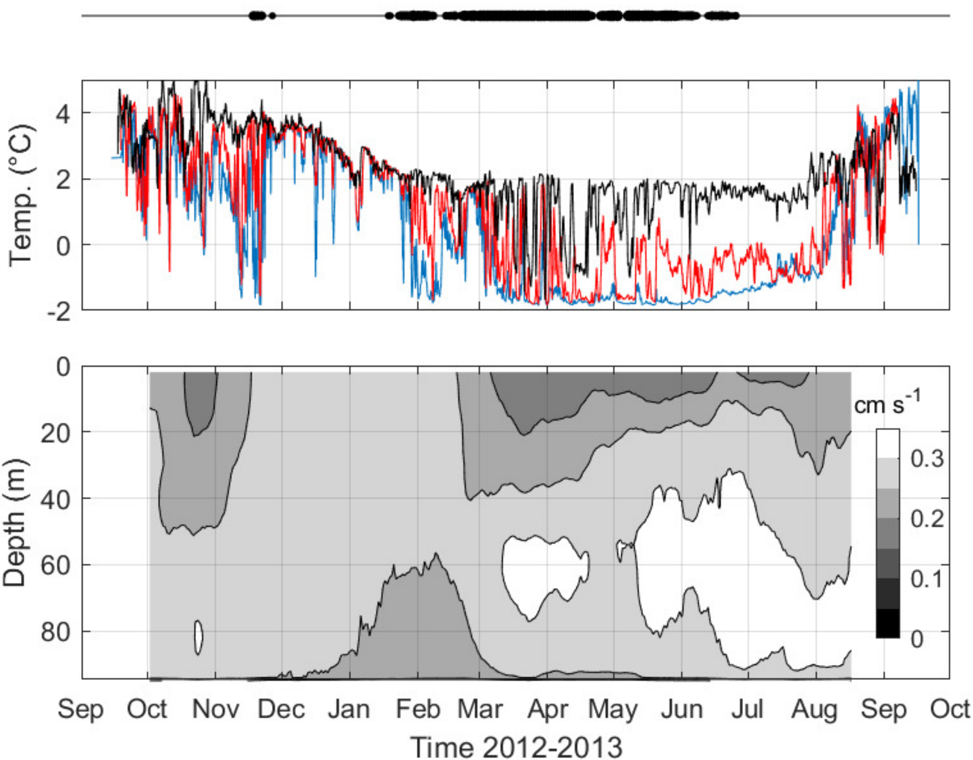

Temp. (°C)
4
2
0
-2
0
20
40
60
80
Depth (m)
cm s-1
0.3
0.2
0.1
0
Sep
Oct
Nov
Dec
Jan
Feb
Mar
Apr
May
Jun
Jul
Aug
Sep
Oct
Time 2012-2013

**Figure 9.**

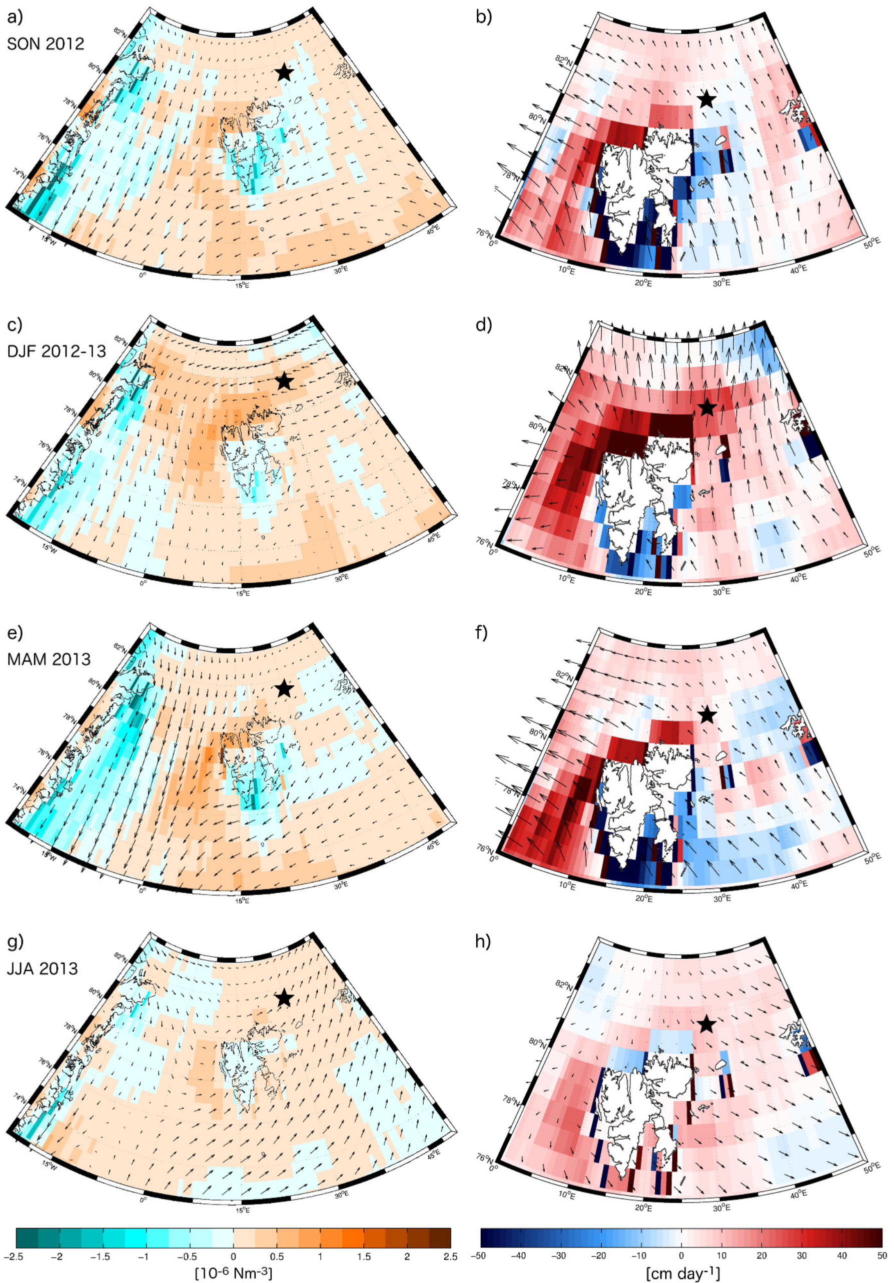

a)
SON 2012
b)
c)
DJF 2012-13
d)
e)
MAM 2013
f)
g)
JJA 2013
h)
82°N
80°N
78°N
76°N
74°N
15°W
0°
15°E
30°E
45°E
10°E
20°E
40°E
50°E
-2.5
-2
-1.5
-1
-0.5
0
0.5
1
1.5
2
2.5
[10^-6 Nm^-3]
-50
-40
-30
-20
-10
0
10
20
30
40
50
[cm day^-1]

**Figure 10.**

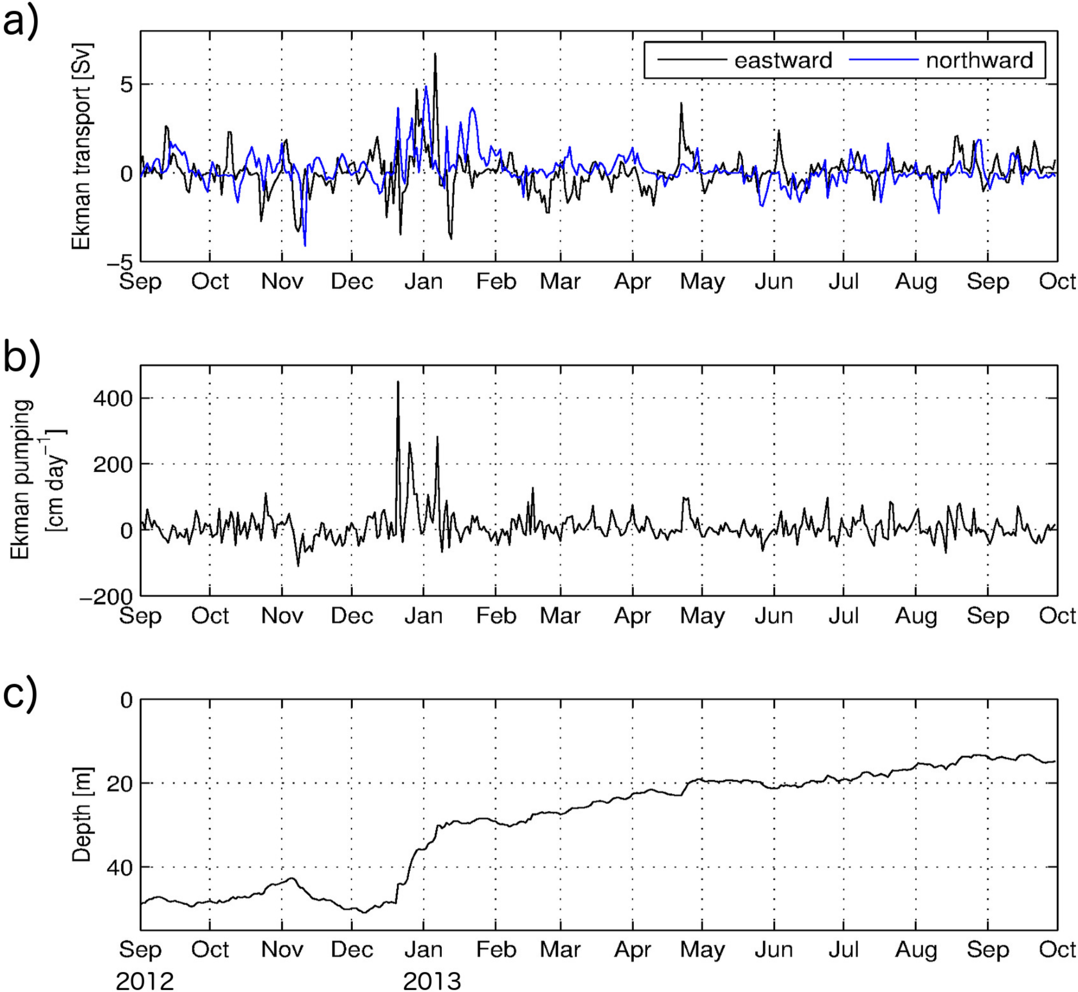
a)
b)
c)
Ekman transport [Sv]
eastward
northward
5
0
−5
Ekman pumping
[cm day$^{-1}$]
400
200
0
−200
Depth [m]
0
20
40
Sep
Oct
Nov
Dec
Jan
Feb
Mar
Apr
May
Jun
Jul
Aug
Sep
Oct
2012
2013

**Figure 11.**

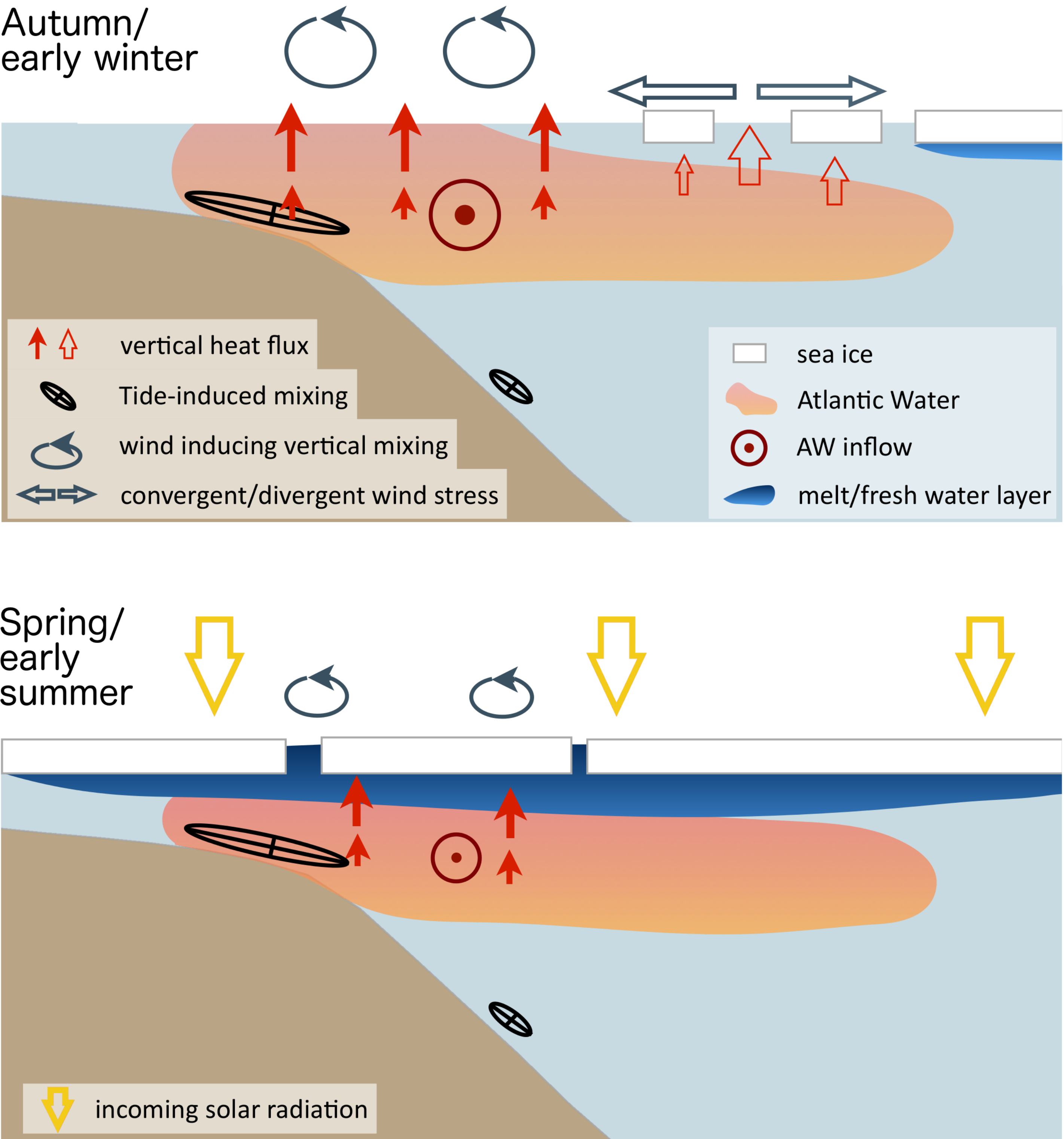

Autumn/
early winter
vertical heat flux
Tide-induced mixing
wind inducing vertical mixing
convergent/divergent wind stress
sea ice
Atlantic Water
AW inflow
melt/fresh water layer
Spring/
early
summer
incoming solar radiation